CNRS

Centre National de la Recherche Scientifique

INFN

Istituto Nazionale di Fisica Nucleare

The Noise Budget of Virgo+ with Monolithic Suspensions

VIR-0677E-09

Date: May 25, 2010

AUTHORS

V.Fafone, I.Fiori, E.Genin, A.Gennai, D.Huet, M.Mantovani, P.Puppo, A.Rocchi, B.Swinkels, E.Tournefier, G.Vajente,

and

The Virgo Commissioning Team

VIRGO * A joint CNRS-INFN Project

Via E. Amaldi, I-56021 – S. Stefano a Macerata - 56021 Cascina, Italia.

Secretariat: Telephone.(39) 050 752 521 * FAX.(39) 050 752 550 * e-mail virgo@virgo.infn.it

Abstract

This document aims to describe and give a tentative projection of the noises expected to contribute to the sensitivity of the Virgo+ detector including the Monolithic Suspensions (Virgo+MS). Individual technical noises are discussed and modeled; their projection is compared to the Virgo+MS design curve. This comparison permits to better define the challenges of the MS detector, and to identify possibly needed noise reduction studies and investigations which are to be pursued before the MS installation.

Table of Contents

1 INTRODUCTION 4

2 LONGITUDINAL CONTROL NOISE 6

3 ANGULAR CONTROL NOISE 8

3.1 AA control scheme during VSR2 8
3.2 Noise propagation 10
3.3 Limitations 11
3.4 Radiation pressure effects 13
3.5 Noise propagation 14

4 THERMAL COMPENSATION SYSTEM NOISE 15

4.1 Evaluation of thermal effects in Virgo+MS 16
4.2 TCS noise projections 17
4.2.1 Compensation to 1000ppm residual coupling losses 18
4.2.2 Compensation to 60ppm-190ppm residual coupling losses 19
4.2.3 Coating absorptions two times higher than expected (2.5ppm) 20

5 NOISE FROM DIFFUSED LIGHT 21

5.1 The mechanism of diffused light noise 21
5.2 Diffused light noise from external benches 21
5.3 Projections for Virgo+MS 23
5.3.1 End benches 23
5.3.2 External detection bench 25
5.3.3 External injection bench 27
5.4 Effect of micro-seism in Virgo+MS 27
5.5 Other back-scattering locations 28
5.5.1 Detection tower output windows 28
5.5.2 Optical Mounts on Suspended Detection Bench 29
5.5.3 Cryogenic trap 29

6 ACTUATORS NOISE 30

7 MAGNETIC NOISE 35

7.1 Introduction 35
7.2 Magnetic noise projections 35
7.2.1 Far-field injections 35
7.2.2 Near-field injections 36
7.2.3 Noise projection using long coherence 37
7.3 Reducing the coupling between mirror and magnetic field 38
7.3.1 Magnet replacement 38
7.3.2 Reference mass 39
7.4 Sources of magnetic noise 39
7.4.1 Electronic racks 40
7.4.2 Mode cleaner air-conditioning 40
7.4.3 UPS noise 40
7.5 Conclusion 41

8 NOISE FROM INPUT BEAM JITTER 42

9 FREQUENCY NOISE 44

9.1 Frequency noise and B5 44
9.2 Coupling of frequency noise 44
9.2.1 Losses asymmetry 44
9.2.2 Finesse asymmetry 45
9.3 Frequency noise projection for Virgo+MS 45

10 PHASE NOISE 47

11 CONCLUSIONS 48

1 Introduction

Figure 1.1 shows a typical noise budget of October 2009. We have achieved a quite good understanding of the sensitivity curve of the *Virgo+* first phase (with 17 W of input power and thermal compensation of input mirrors). We have succeeded to reduce major technical noises below fundamental ones, and the sensitivity is now limited by only known sources. Major technical noises have been identified and their projection is reconstructed through a model or a measured transfer function [1].

The next detector upgrade phase consists of the installation of new mirrors with Monolithic Suspensions. The new detector (here we name it *Virgo+MS*) foresees a significant reduction of the thermal noise and increased sensitivity in the region below 100Hz (factor 3 to 7 with respect to Virgo+ design). Figure 1.2 compares the Virgo+ and Virgo+MS design curves [2, 3]. The sight range for NS-NS inspiral events will increase from 13Mpc (Virgo+) to 47Mpc [2, 3]. It is important to understand if technical noises are compliant with this challenge.
The fundamental noises of Virgo+MS (thermal noises, quantum, seismic, gravity gradient and residual gas), the new detector parameters and the new design curve are described in a separate document [3]. In this document we discuss all identified technical noises which are expected to contribute to Virgo+MS detector sensitivity. One Chapter is dedicated to each noise (Chapters 2 to 10). For each noise the current understanding of the noise is illustrated and a projection to the Virgo+MS detector is presented and motivated. The noise reduction strategy, if necessary to comply with the design curve, is presented and its feasibility is discussed. Investigation studies and activities to pursue during the MS preparation phase are thus identified and described. Finally the full noise budget is compiled and discussed (Chapter 11).

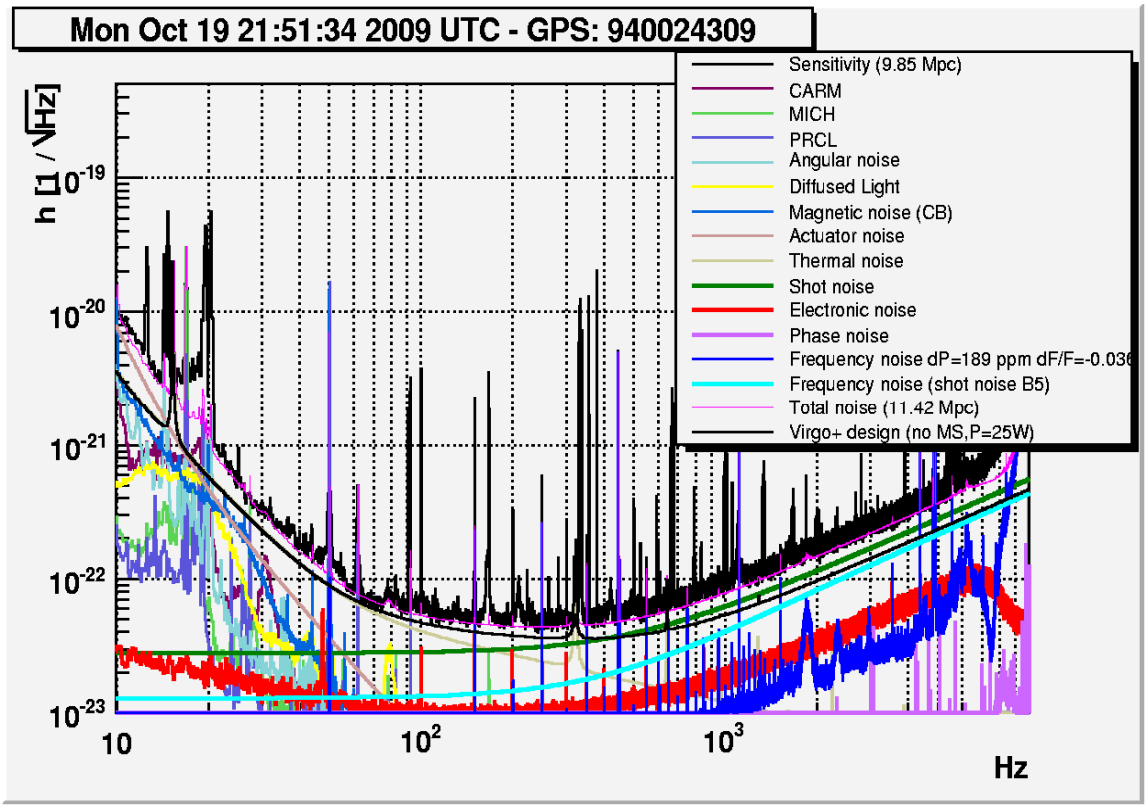

Figure 1.1. Recent noise budget with input power P0=17 Watts and thermal compensation. The total noise (pink curve) also includes the expected thermal (pendulum and mirror) noises. The Virgo+ design curve is computed with the updated SA thermal noise model and with P0=25Watts, F=50 and Rc=43.

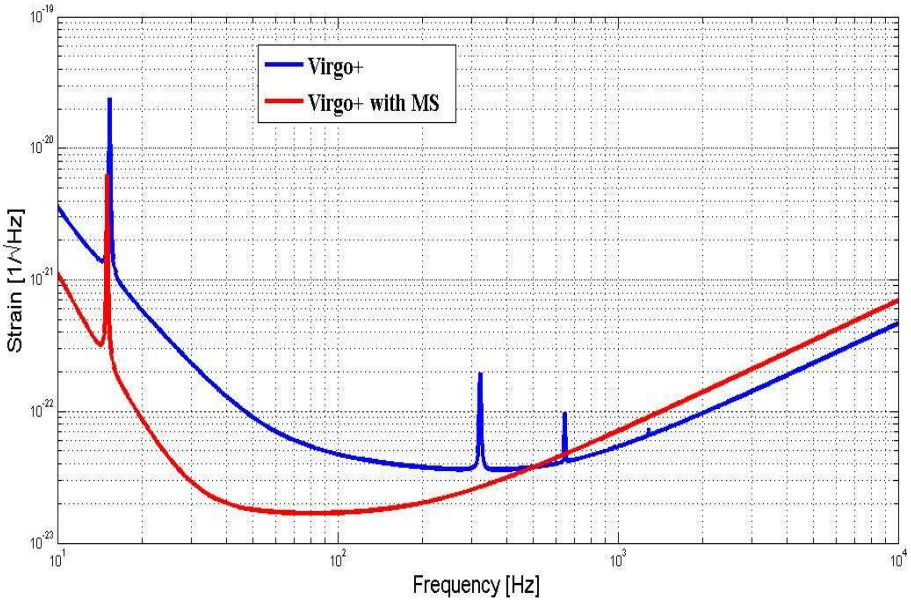

Figure 1.2. Virgo+ (blue) and Virgo+MS (black) design curves, as from reference [2]. The Virgo+ curve uses P0=25Watts, F=50 and Rc=43; the Virgo+MS curve uses P0=25Watts, F=150 and Rc=20. The sight range computed for NS-NS of 1.4 solar masses with these curves is 12.8Mpc for Virgo+ and 47Mpc for Virgo+MS.

2 Longitudinal control noise

A reasonable estimate of the longitudinal control noise contribution to Virgo+MS noise can be obtained with the following assumptions:

- the same control scheme will be used for the locking of Virgo+ and Virgo+MS [4];
- presently longitudinal control noise is limited by photo-diode sensor noises which will remain the same for Virgo+MS. This is conservative, since noise hunting efforts should help in improving them;
- the same performances of noise subtraction (alpha, beta and gamma) will hold in Virgo+ and Virgo+MS.

Given these assumptions, we can consider the present measured noise projections for Virgo+ and reduce the MICH and PRCL contribution by a factor 3. This comes from the (simulated and measured) fact that the coupling of these two auxiliary degree of freedom residual motions scales with the arm cavity finesse. Figure 2.1 shows the detailed contribution and Figure 2.2 shows the total noise compared to Virgo and Virgo+MS design sensitivities.

It is clear from the figures that MICH and PRCL control noises will be compliant with Virgo+MS design sensitivity, except for a few structures around 30-40 Hz, which are of environmental nature. Note that the structures around 20 Hz are calibration lines.
The main contribution to control noise will come from the CARM loop, which is presently locked on the reference cavity with 1.5Hz bandwidth. This error signal is quite noisy and if no improvement can be made it will be the dominant contribution and will strongly limit Virgo+MS sensitivity.
However experiments are already being carried out to reduce this loop bandwidth down to 200mHz [5]. This new strategy seems feasible and it will completely remove CARM contribution to longitudinal control noise, at the level shown by the blue curve in Figure 2.2.

In conclusion, assuming the same level of sensor noise we have now in Virgo+, longitudinal control noise will give a contribution below the Virgo+MS design sensitivity, assuming a better CARM control strategy, except around few structures of environmental origin.

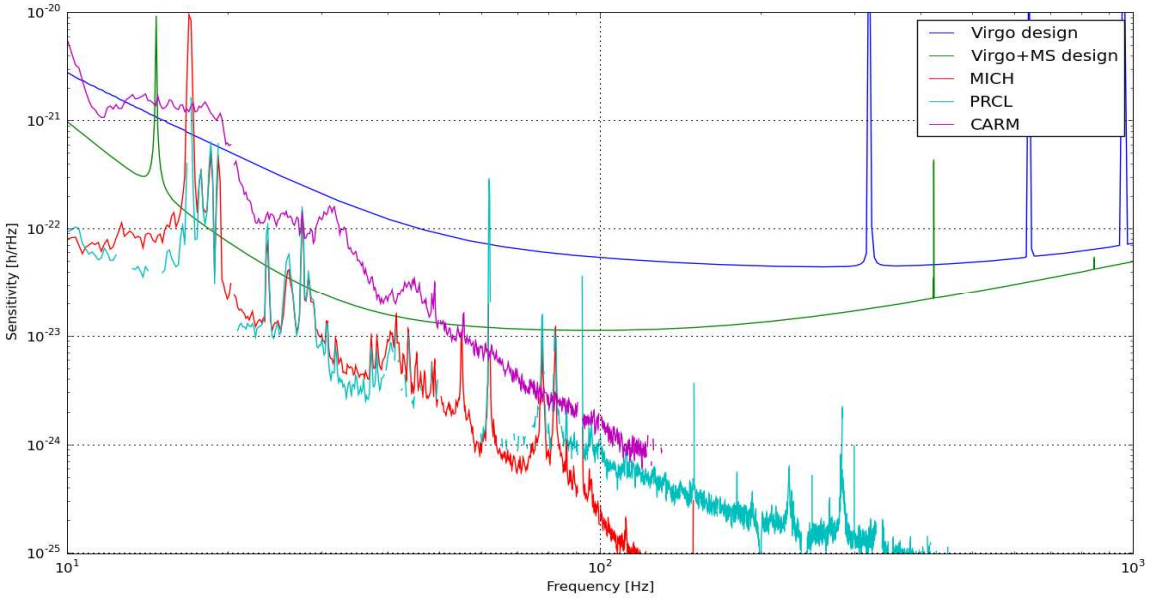

Figure 2.1. Projection of longitudinal control noise for Virgo+MS, individual contributions.

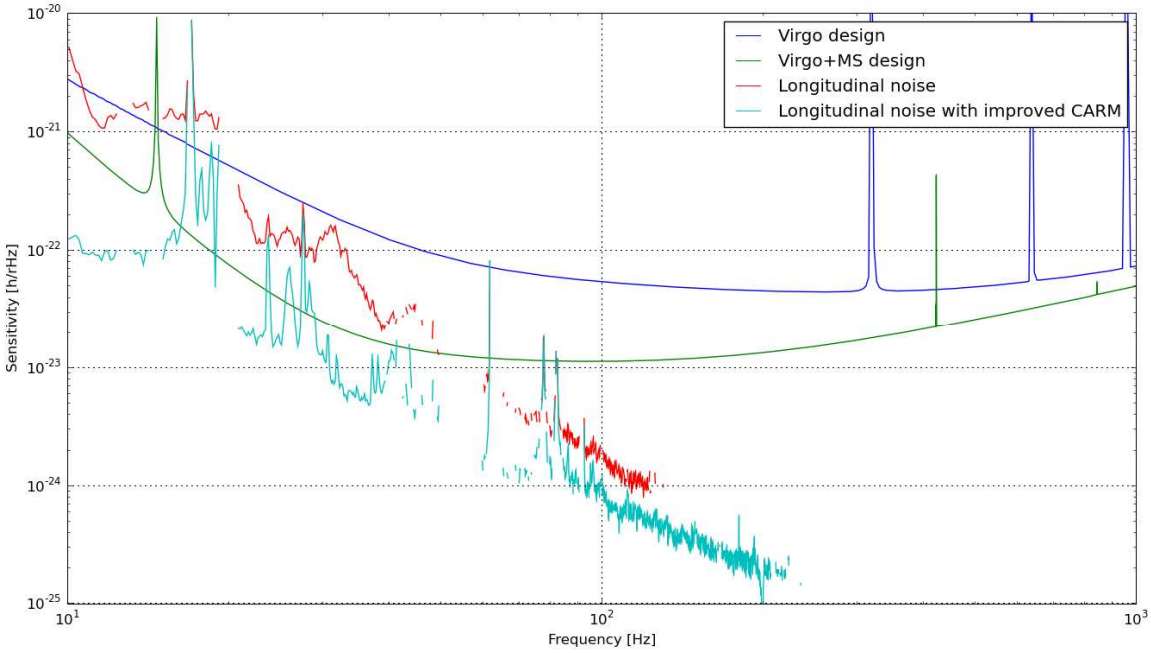

Figure 2.2. Total longitudinal control noise expected for Virgo+MS assuming the same control strategy or an improved one for CARM.

3 Angular control noise

In order to be able to evaluate the effect of the Automatic Alignment control noise in the Virgo+MS configuration, considering also the monolithic suspension installation, the control chain has been simulated and the control noise has been projected to the Virgo+MS design sensitivity.
The supposition taken into account in the following analysis, to be able to obtain realistic performances, is that the control chain for Virgo+MS will be improved only in the sensing part thanks to the installation of the new electronics and the optimization of the amount of impinging power on the quadrant diodes.
The propagation of the electronic/shot noise in the Automatic Alignment control loop chain is computed by using *Matlab* scripts, modeling the electronics, the control and the mechanics in the frequency domain, while for the transfer functions of the angular d.o.f. to the sensitivity the measured transfer functions have been considered.

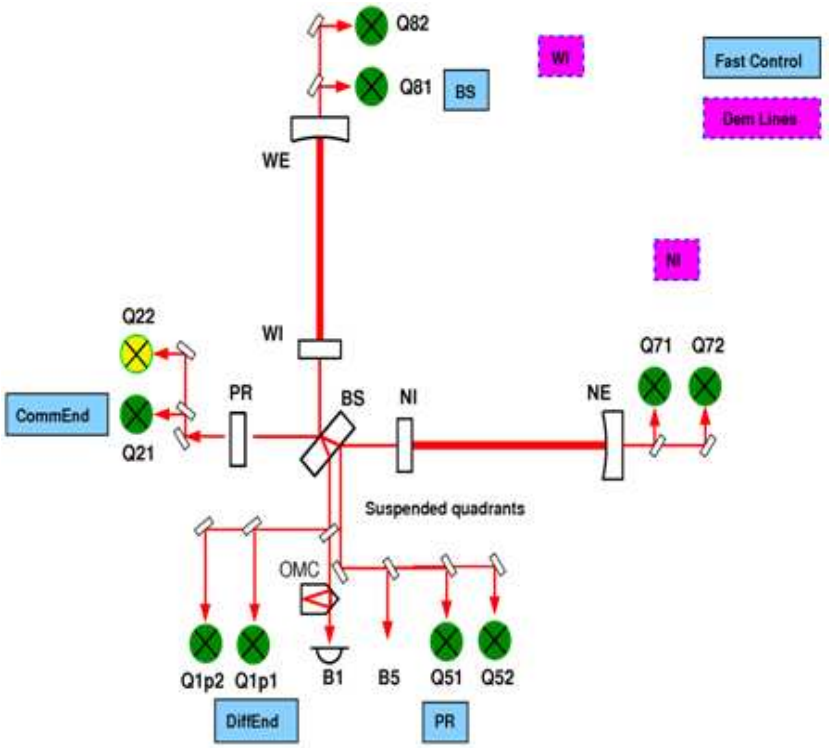

Figure 3.1. Initial Automatic Alignment control scheme for VSR2

3.1 AA control scheme during VSR2

The angular control scheme during VSR2 is shown in Figure 3.1. The control is based on a mix of fast control, with a bandwidth of few Hz, for the Common Differential End, PR and BS modes and slow control, called Drift control with a bandwidth of some mHz for the input mirrors.

The Drift control consist in the modulation and demodulation of the input mirror angular displacement with frequencies below the detection band, from 7 to 9 Hz, to steer and center the beam on the terminal mirrors minimizing the longitudinal/angular coupling.
The most critical d.o.f. for noise performances are the ones which are controlled with the large bandwidth thus in the following only these degrees of freedom will be taken into account.
During VSR2 an improved control scheme has been implemented, which swaps the control of the *CommEnd* mode from the Q21 DC signal, which is strongly dominated by the EIB seismic motion at high frequency (above 10Hz) and by air current in the control bandwidth, to a combination of the suspended quadrants, on the suspended detection bench, DC signals.
The accuracy of the control has been improved by a factor ~3 and the error signal high frequency noise is lowered in the 10-20Hz region.
The current performance of the Automatic Alignment system fulfils the Virgo requirements for any frequencies in the detection band, as it is shown in Figure 3.1.

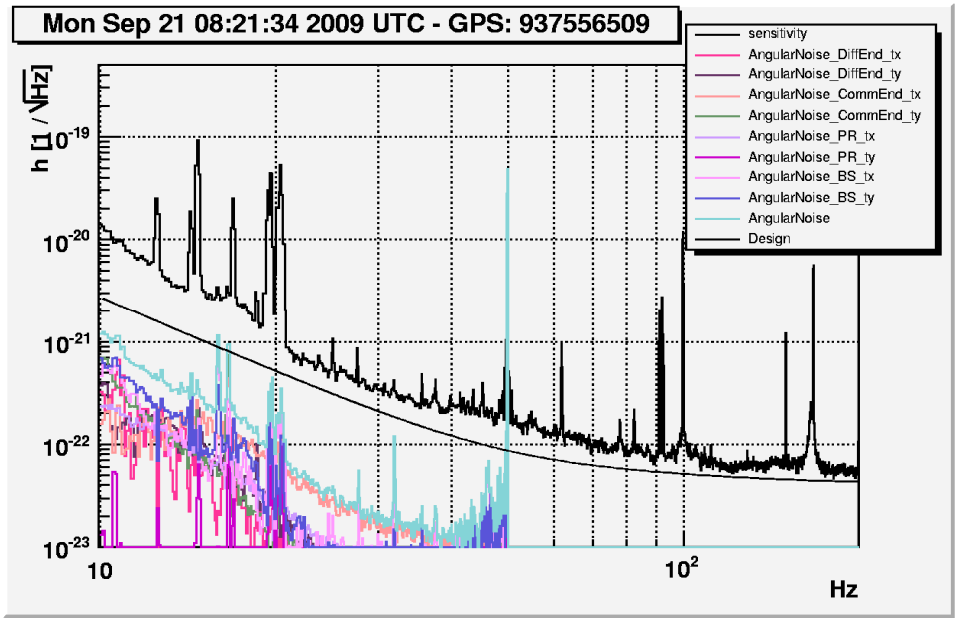

Figure 3.1. Automatic Alignment noise budget during VSR2.

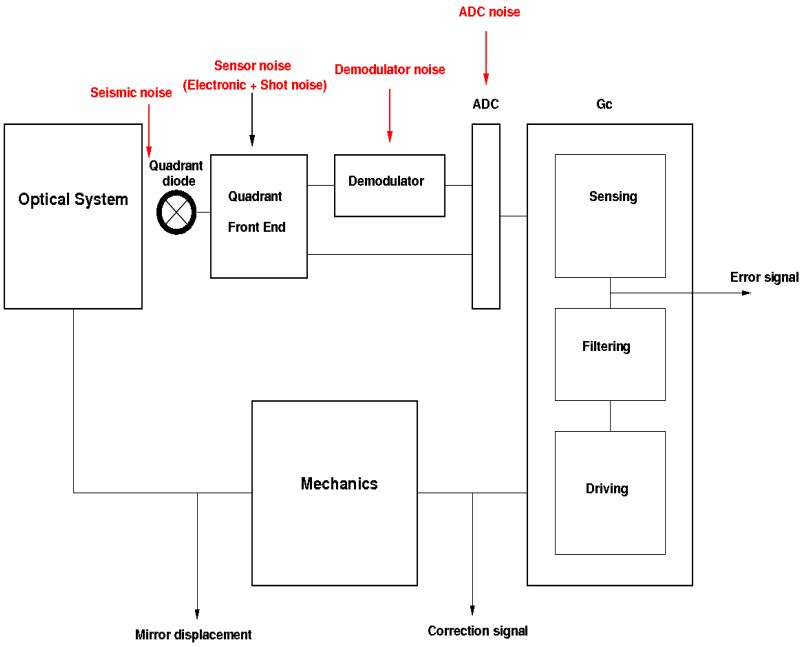

Figure 3.2. Automatic Alignment control chain, the noises are highlighted in red.

3.2 Noise propagation

In order to evaluate the contribution of the Automatic Alignment control noise to the Virgo+MS sensitivity the control chain has been modeled by using *Matlab* scripts, considering four different sources of noise:

- Environmental noise, seismic noise of the detection benches which affects the DC error signals (the measured seismic motion spectra have been used);
- Front-End noise, electronic-shot noise of the quadrant module;
- Demodulator board noise;
- ADC noise.

A scheme of the control noise simulation chain is shown Figure 3.3.
In order to have the best performance the power impinging on the diodes should be highest as possible, taking account the saturations in the sensing chain the gains of the electronics should be lowest as possible, in order to be limited only by shot noise.
The amount of power impinging on the diodes has been decided in agreement with the DET group. Moreover some margins of safety have been considered in the optimization in order to avoid saturations in the lock acquisition phase, since the RMS of the signals is much higher in this phase with respect to the science mode.

The optimized powers on the diodes are then:

Diode	Actual power [mW]	V+ optimized power [mW]
Q1p	0,0124	0,0160
Q21	0,0950	2,0000
Q51	1,68	5,0000
Q81	0,2700	16,5000

3.3 Limitations

The main limitation for the Virgo+MS sensitivity achievement for the Automatic Alignment control noise is the ADC up-conversion.
The alignment signals have a very large dynamic, of about 10^6, which generates the up-conversion at the level of the ADC, thus the ADC noise which should be a flat noise of ~100nV/√Hz starts to rise as 1/f starting from ~100Hz.
This noise is actually limiting the Q21 and Q1p1 signals, which are used to control the Common and Differential End modes respectively, and it will increase as the error signal to noise ratio will increase since it depends on the signal dynamic.
The other limitation is due to the seismic noise which affects the DC error signals, which was limits the Common End error signal in the initial alignment configuration.

To control the Common End d.o.f. there are two possible control strategies. The first strategy consists in using the q21 DC error signal, the quadrant placed on the external injection bench used in the initial control configuration for VSR2, see Figure 3.4. The alternative is to use a combination of the quadrants placed on the suspended detection bench DC signals, see Figure 3.5.

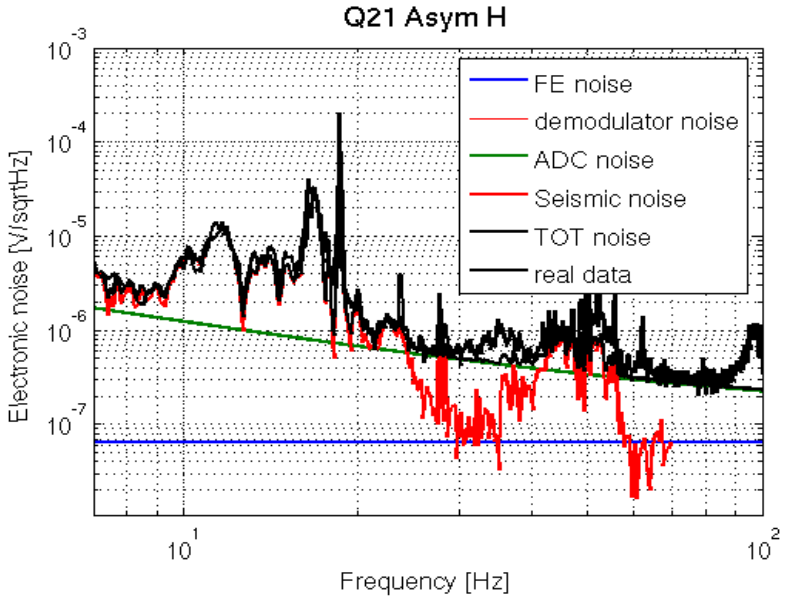

Figure 3.3. Q21 DC high frequency noise for the horizontal channel which is used to control the Common End tx d.o.f. in the initial VSR2 configuration for the AA control scheme. This signal is dominated by the EIB seismic noise, red curve, plus the ADC noise, green curve which is strongly affected by up-conversion.

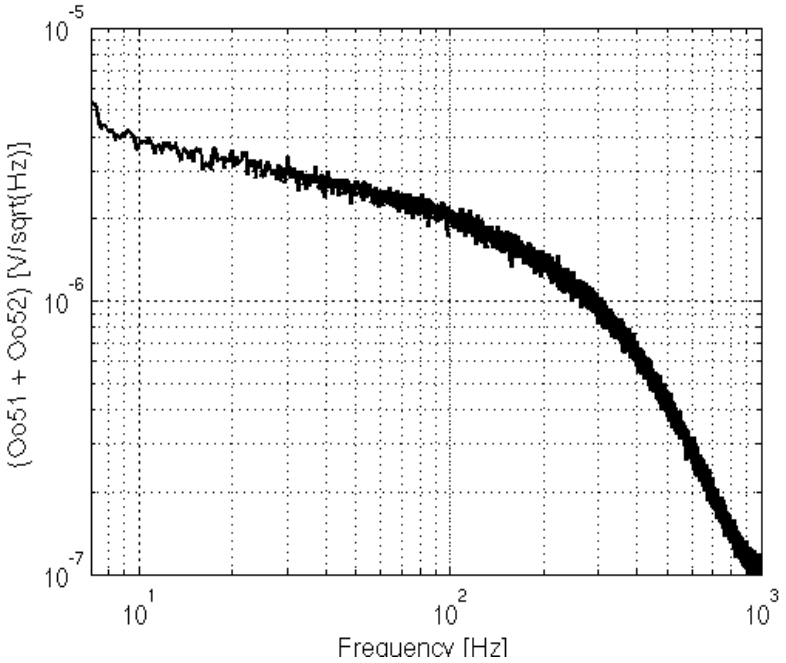

Figure 3.4. High frequency noise of the combination of the suspended quadrants DC signals used to control the Common End d.o.f. in the present configuration for the Automatic Alignment system, the shape of the signal suggests that also in this case the ADC up-conversion is present.

The second configuration, the one which is presently running, has strong vantages such as the better low frequency accuracy, since the error signals are not affected by air current, and no

seismic noise at high frequency, but still the error signal electronic/shot noise is too high for the Virgo+MS requirements.

The idea is to maintain the control of the Common End d.o.f. at low frequency, up to some Hz, by using the suspended quadrants, to profit of the better accuracy and then use at high frequency, by mixing the signals if necessary, the most performing signal in term of noise.
In order to reach the design sensitivity for V+ the ADC up-conversion has to be solved, and if it will be solved only a factor of ~5 of improvement on the suspended quadrants noise can be reached.
While to improve the Q21 noise, apart from the ADC up-conversion reduction, the EIB has to be suspended.
The first option, using the suspended quadrants, will not be enough if a factor 10 of safety below the design sensitivity has to be considered since the Common End control noise will be 2e-22 at 10 Hz, while if the Q21 DC error signal will be used the signal to noise ratio can be improved by increasing the amount of light impinging on the diode.
For the environmental noise reduction on Q21 the suspension of the bench has already been planned while the ADC up-conversion is still under studies.

3.4 Radiation pressure effects

The major difference between the Virgo+ and the Virgo+MS configurations, apart from the better sensitivity, is the higher circulating power, of about 45kW. This could produce strong radiation pressure effects on the mechanical resonant frequencies of the cavity. As shown in Figure 3.5, the system remains stable and not critical.

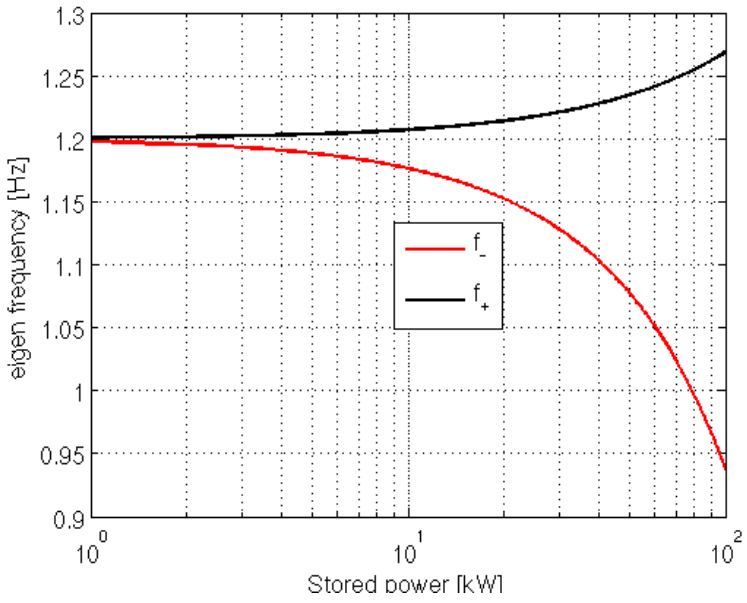

Figure 3.5. Radiation pressure effects on the resonant frequencies, the system remains stable.

3.5 Noise propagation

The control noise has been then modeled and propagated in the control chain to the Virgo+MS sensitivity. The analysis has been done considering that the seismic excess of noise on the Q21 DC signal and the ADC up-conversion has been solved.
As it is shown in Figure 3.7 and Figure 3.8, the simulated control noise is well below the design sensitivity of Virgo+MS, in accord to the safety margin of a factor 10.
The only concern is that if the ADC up-conversion can not be solved, the behavior of the up-conversion has to be evaluated as a function of the dynamic of the signal in order to have a more realistic simulation.

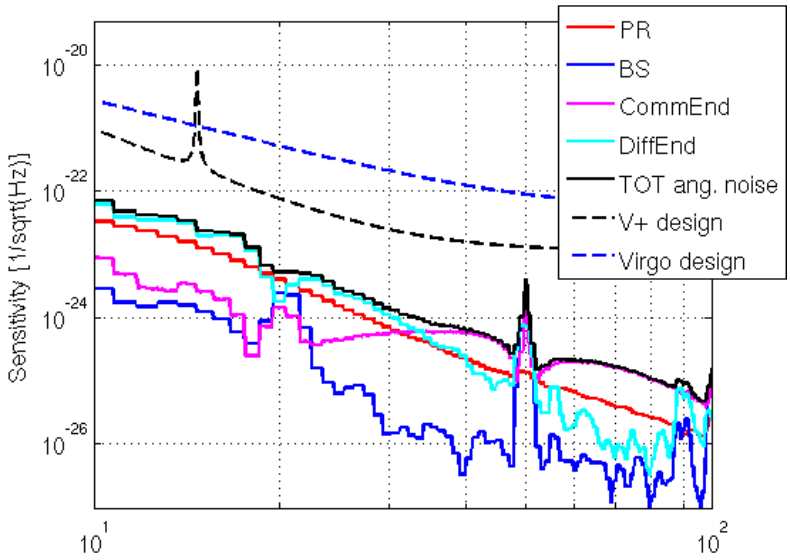

Figure 3.6. Simulated control noise for the Tx direction.

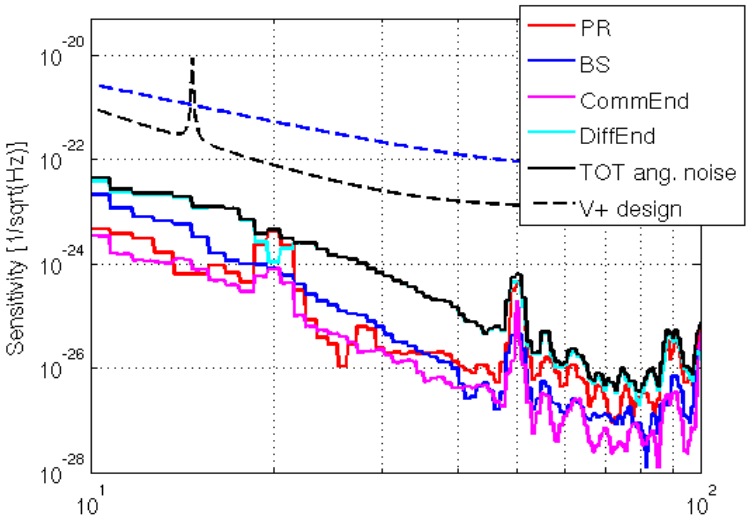

Figure 3.7. Simulated control noise for the Ty direction.

4 Thermal Compensation System noise

The TCS installed in Virgo is based on a pre-stabilized CO_2 laser projector that shines a heating pattern onto the HR surface of each input mirrors.
The TCS system can convert the intensity noise of the CO_2 laser into displacement noise through several mechanisms:

- Radiation pressure;
- Thermo-elastic: fluctuations in locally deposited heat cause fluctuations in local thermal expansion;
- Thermo-refractive: fluctuations in locally deposited heat cause fluctuations in local refractive index ;
- Flexure: fluctuations in locally deposited heat cause fluctuations in *global* shape of the optic.

A detailed treatment of TCS noise couplings can be found in [6] and references therein. In case of annular heating, the flexure noise is by far the dominant contribution and the expression for the strain is given by:

$$h_{TCS} = \frac{P}{2\pi f C \rho} \frac{6\alpha}{h^2} C_{num} \frac{RIN}{L}$$

where P is the TCS power, C, ρ, α, h are respectively the heat capacity, the density, the linear thermal expansion coefficient and the thickness of the test mass. RIN is the CO_2 laser relative intensity noise and C_{num} describes the coupling of the flexure noise, f is the frequency and L the arm cavity length. Besides the geometrical factors included in C_{num}, the noise introduced by the TCS depends on the power required for compensation and the CO_2 laser noise.
A comparison between the theoretical TCS noise transfer function (normalized to the CO_2 laser noise) and the measurements is shown in Figure 4.1. The experimental curve has been estimated by G. Vajente (see logbook entries n. 23829 and n. 23830) while the theoretical curve has been calculated using the formula above. The comparison shows a good agreement between calculation and measurement, thus confirming the previous cross-check made using a different method suggested by E. Tournefier (see logbook entry n. 20475 and [6]).

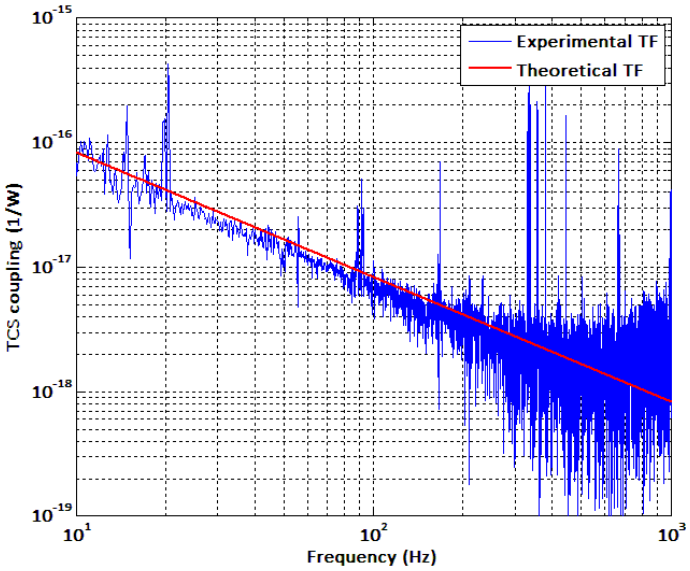

Figure 4.1. Comparison between the theoretical TCS noise transfer function and the measured one.

4.1 Evaluation of thermal effects in Virgo+MS

To have a quantitative estimate of thermal effects in Virgo+MS, a precise knowledge of the new ITMs coating and substrate absorptions is necessary. As these measurements, at present, have not yet been performed on the new input mirrors, we considered confident values those measured at LMA on the Virgo ITMs: 1.25ppm for the coating [7, 8] and 0.7ppm/cm for the substrate [9, 10]. Even if recently [11] a value of 0.6ppm has been measured for the coating absorption, we considered 1.25ppm in order to be conservative. Thus, with a Finesse of 150, a recycling gain of 20 and an input power of 25W, the amount of thermal effects without TCS is expected to be around 2400ppm, in terms of coupling losses, defined as [12]:

$$L = 1 - |\gamma|^2 \quad \text{with} \quad \gamma = 2\pi \int_0^a e^{ikZ(r)} |\Psi(r)|^2 \, r \, dr$$

where a is the radius of the test mass, $Z(r)$ the optical path length increase, k is the wave number and $\Psi(r)$ is the power density of the YAG beam. As a reference, the residual coupling losses, calculated for VSR2 with TCS on, amount to approximately 4000ppm.
The performances of the TCS have been simulated as a function of the annulus inner radius and CO_2 power, the outer radius has been kept at 14cm, equal to the present value. Results are shown in Figure 4.2.

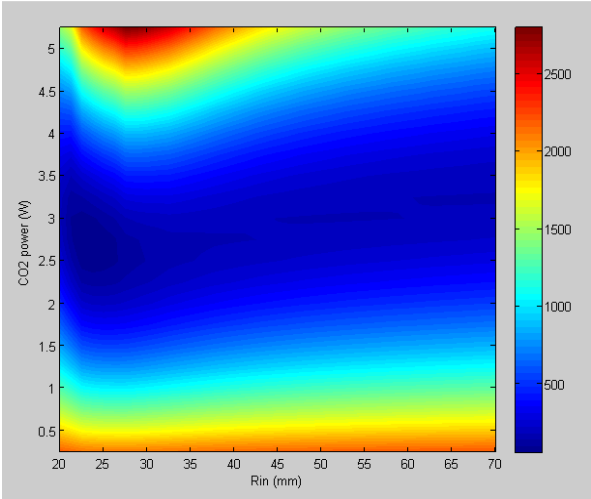

Figure 4.2. Coupling losses as a function of the inner radius of the annular heating beam and of the CO2 power.

The minimum of the coupling losses is about 60ppm for 2.5W of power and R_{in}=25mm; this is the inner radius that has been used during the first tests on the TCS (the corresponding heating pattern is shown in the left image of Figure 4.3). Before starting VSR2, the inner radius has been increased to R_{in}=70mm (see right image in Figure 4.3). For this value there is a relative minimum of the coupling losses of 190ppm for 3.3W. We also considered a reduction of a factor of two of the thermal effects wrt the uncompensated case, i.e. 1000ppm residual coupling losses: for the two values of inner radius considered, approximately 1.0W and 1.3W of TCS power respectively are needed. TCS noise has been evaluated for these possible compensation levels.

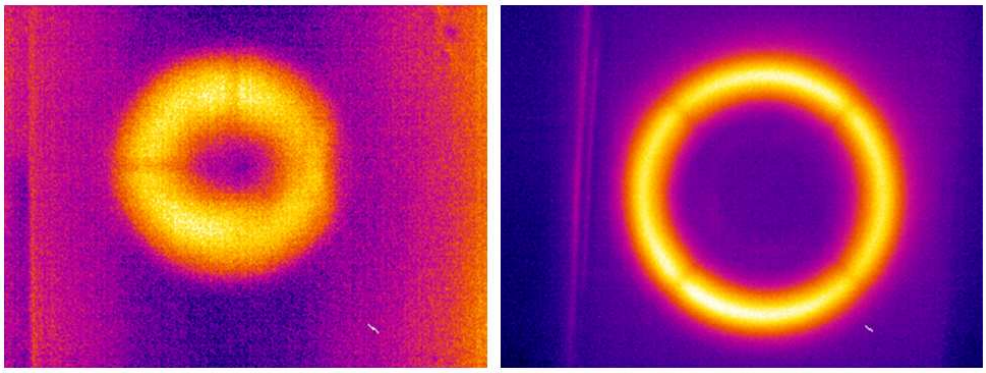

Figure 4.3.Thermal images of heating patterns with Rin=25mm (left) and Rin=70mm (right).

4.2 TCS noise projections

The two values of the inner radius considered in the previous section have been used to calculate the corresponding values of C_{num}, reported in Table 4.1.

R_{in} (mm)	C_{num}
25	0.135

70	0.074

Table 4.1. Geometrical parameters used for the evaluation of the TCS noise.

The other necessary parameter to compute the TCS contribution to Virgo+MS sensitivity is the relative intensity noise of the CO_2 laser. At the beginning of October, after the studies carried on in Tor Vergata Laboratory [13], the intensity stabilization loop has been installed on the site (see Logbook entries # 25132 and 25196). The closed and open loop noise spectra are shown in Figure 4.

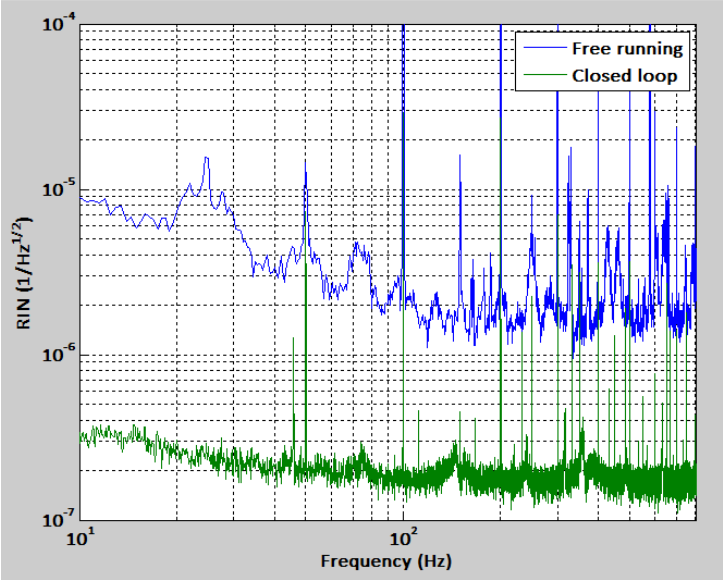

Figure 4.4. Open loop (blue) and closed loop (green) CO2 laser noise spectra

4.2.1 Compensation to 1000ppm residual coupling losses

In this case, as stated above, the TCS powers required are about 1.0W and 1.3W for a small and large hole respectively. Figure 4.4 shows the corresponding TCS noise projections, the blue and green curves refer to the CO_2 laser noise measured in Virgo, while the red curve represents the TCS noise evaluated for a flat *RIN*, averaging the floor of the laser noise spectrum.

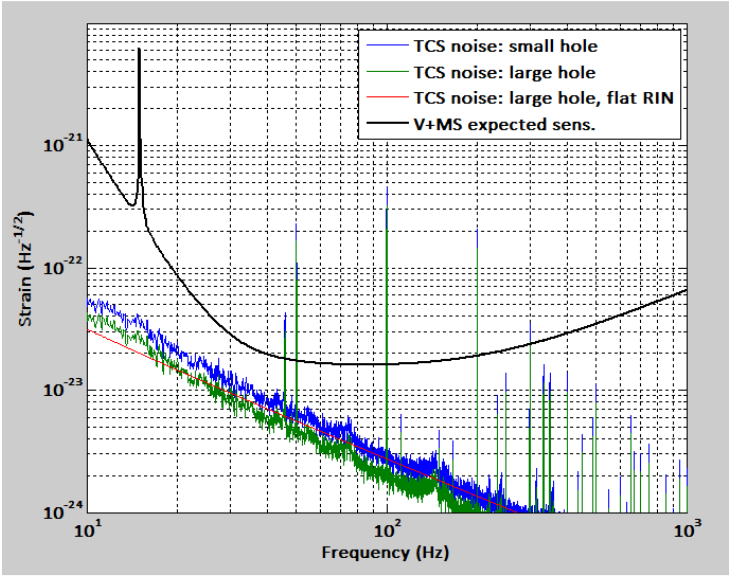

Figure 4.4. TCS noise projections compared to the Virgo+MS expected sensitivity curve.

Looking at the graph above, we can conclude that in this configuration, the TCS noise is safely below the Virgo+MS expected sensitivity at all frequencies.

4.2.2 Compensation to 60ppm-190ppm residual coupling losses

In this case, the TCS power required are 2.5W and 3.3W for R_{in}=25mm and R_{in}=70mm respectively. Figure 4.5 shows the corresponding TCS noise projections.

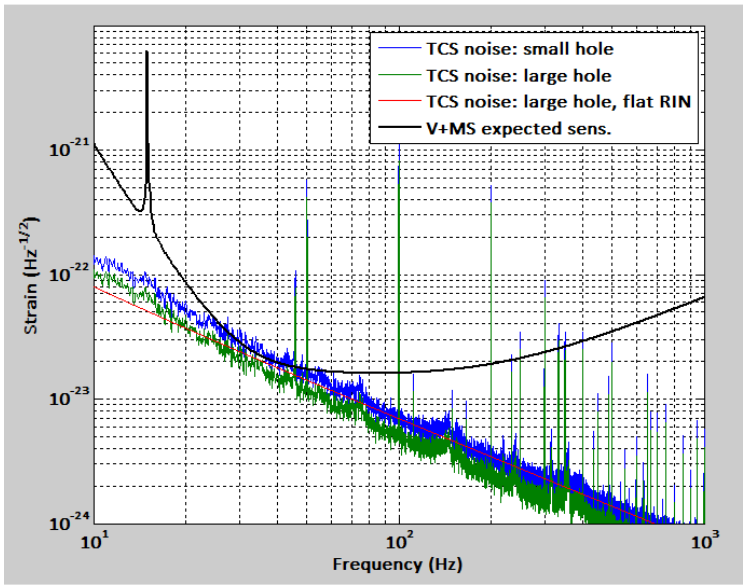

Figure 4.5. TCS noise projections compared to the Virgo+MS expected sensitivity curve.

For this compensation configuration, the TCS noise contribution to the Virgo+MS expected sensitivity is not negligible. A reduction of the CO_2 laser noise of a factor of 3-4 is necessary.

This could be accomplished by increasing the number of in-loop photodiodes to 9-16. In fact, the SNR scales as $\sqrt{N}$, where N is the number of photodiodes.

4.2.3 Coating absorptions two times higher than expected (2.5ppm)

The case of coating absorptions higher than expected has also been considered. In this scenario, coupling losses with no TCS would amount to 8000ppm. Again we studied both cases: reduction of coupling losses to the minimum values (optimal compensation) and reduction to half of the uncompensated value, i.e. 4000ppm (same as during VSR2). In case of optimal compensation, the required TCS power is 5.5W for inner radius of 25mm (residual losses of 230ppm) and 6.5W for an inner radius of 70mm (residual losses of 700ppm). Reducing coupling losses to 4000ppm decreases the power needed to compensate by more than a factor of two: 2.1W for R_{in}=25mm and 2.6W for R_{in}=70mm.

Optimal compensation in case of absorptions two times higher than expected is not feasible since a further reduction of the CO_2 laser intensity noise of a factor of 10 would be necessary.

The case of VSR2-like compensation seems feasible (see Figure 4.6), provided a reduction of the CO_2 intensity noise of a factor of 3-4 is obtained by increasing the number of photodiodes to 9-16.

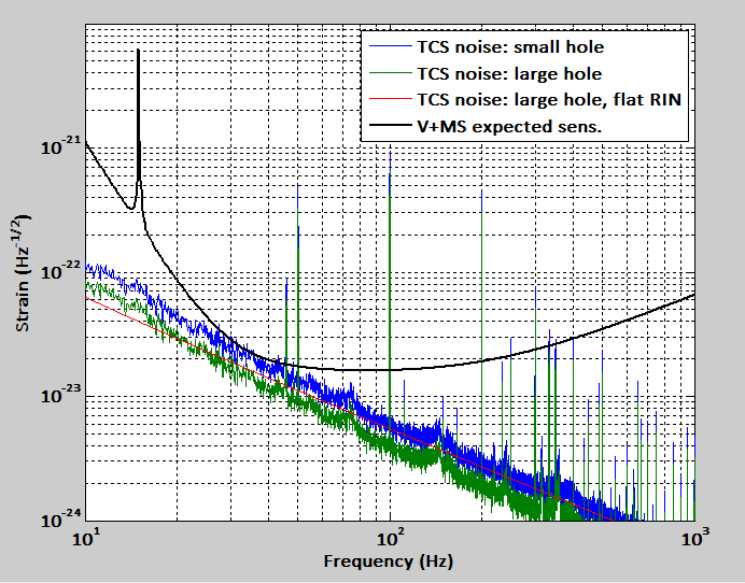

Figure 4.6. TCS noise projection for VSR2-like compensation with 2.5ppm coating absorptions.

5 Noise from diffused light

5.1 The mechanism of diffused light noise

Diffused light processes can couple seismic noise from the external environment into the interferometer. A fraction of beam power which impinges on vibrating surfaces (e.g. lens, beam dump, optical mount, optical window, vacuum tank inner walls) can be scattered back and recombine with the main beam. This type of noise is found relevant for frequencies below about 200 Hz, where the environmental seismic vibration is larger.
The noise produced in the gravitational wave signal by a generic diffused light source can be parameterized as [14]:

(Eq.5.1) $$h_{bs}(t) = G\sin(\frac{4\pi}{\lambda}x(t))$$

where, *x(t)* is the surface motion along the scattered beam direction, the quantity in parenthesis is the phase noise carried by the back scattered beam. The "coupling factor" *G* can be expressed as:

(Eq.5.2) $$G = K\sqrt{f_{sc}}$$

where, f_{sc} is the fraction of light beam power impinging on the scattering object that is scattered back into the ITF opening angle, and *K* is a parameter that depends on the location of the scattering, and on ITF optical parameters.

As can be deduced from Eq.5.1, the coupling of diffused light is highly non linear in case of large displacements, typically for $\Delta x_{opt} > \lambda/4\pi$. Therefore if the scattering source is moving with a large amplitude (A_x) at low frequency (f_x < 1Hz) it can still spoil the Virgo sensitivity above 10Hz. If the amplitude of the displacement remains below $\lambda/4\pi$ harmonics of the main seismic peaks frequency show up in *h,* but for larger displacements an almost flat spectrum appears, up to a maximum frequency f_{max} with a rapid fall-off above f_{max} [14]:

(Eq.5.3) $$f_{\max} = \frac{2A_x}{\lambda}2\pi\ f$$

5.2 Diffused light noise from external benches

External optical benches are significant sources of back scattered light. The case has been well studied during Virgo commissioning and several mitigations have been performed [15]. For each external bench we have measured and estimated the value of *G*:
we have measured *G* by shaking tests (for more details see Virgo Note [15]);
we have estimated *G* values, based on measured back scattering properties of optic elements on the external beam path (to estimate f_{sc}), and based on ITF optical parameters. This is described in one Virgo note [14].

Table 5.1 lists measured and estimated *G* values for external benches. The good agreement indicates we have reasonably good understanding of diffused light from these benches. This permits to do reliable extrapolations to Virgo+MS, accounting for its different optical parameters.

Figure 5.1 shows the projection of external benches noise during VSR2. In conditions of intense sea activity the up-conversion of the increased microseism (<1Hz) noise spoils the Virgo sensitivity below 100Hz (Left plot in Figure 5.1). This condition, corresponding to an RMS soil displacement (between 0.2Hz and 1Hz) of more than 2microns, occurs about 10% of the time (see one-year statistics of site microseism in Figure 5.2). The dominant contribution is that of diffused light at the WEB (Figure 5.1, left). Which is due to the larger coupling (Table 5.1, column 1) and to the fact that the microseism is about twice as intense at WE because of its closeness to the coast.

	V measured	V expected	Virgo+MS expected	Comment
NEB	1.5	5	0.3	V+ extrapolated from V measured
WEB	23	20	0.9	V+ extrapolated from V measured
EDB	10	10	3	Faraday on B1s for Virgo+MS
DT	20-40	>10	1	Faraday on B1s for Virgo+MS
EIB	<1	negligible	negligible	

Table 5.1. Measured and expected coupling factors G for Virgo and Virgo+MS, for each external bench and the detection output window. Numbers are in units of 10^{-21}.

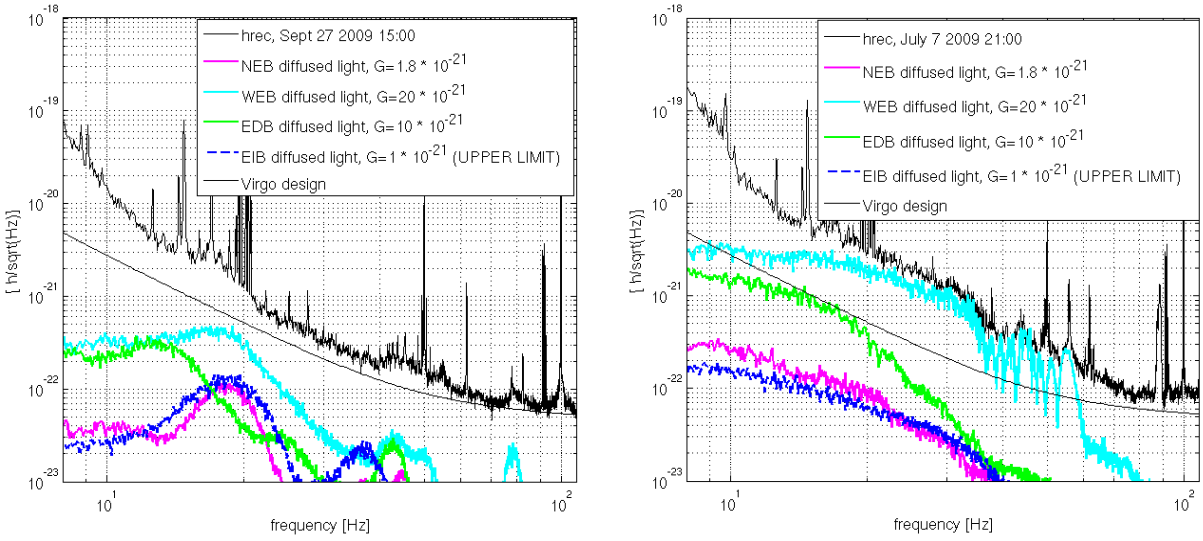

Figure 5.1. Left: Projected diffused light noise contribution from each external bench, during VSR2 in case of low sea condition (70% of time). Right: same in case of large sea activity (a condition present 3% of time during last year).

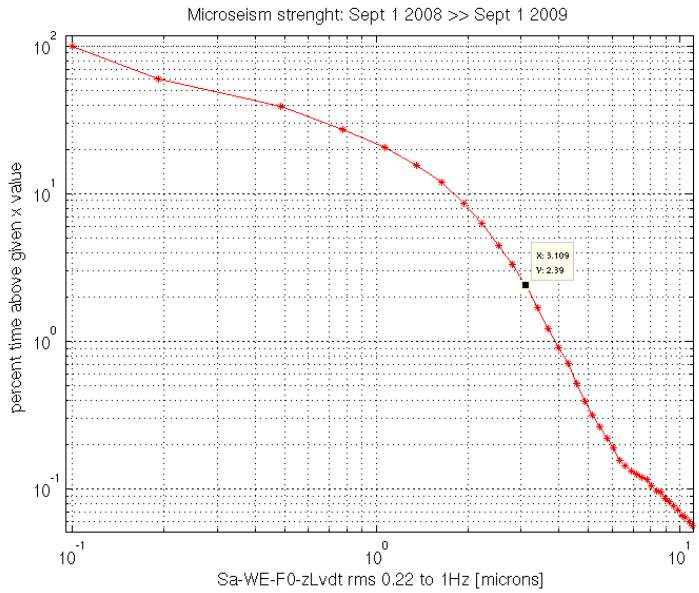

Figure 5.2. One-year statistics of the site microseism activity. On x-axis is the RMS displacement of the top stage of WE mirror super-attenuator between 0.22Hz and 1Hz. At these frequencies the SA top stages moves as the ground. On y-axis is the percent time above a given RMS values.

5.3 Projections for Virgo+MS

5.3.1 End benches

The coupling factor of diffused light from external end benches is:

(Eq. 5.4) $$K_{end} = \frac{\lambda}{4\pi}\frac{T_{end}}{\sqrt{2F\pi}}$$

where, L is the FP cavity length, F is the cavity finesse, and T is the end mirror transmission.
When the monolithic suspensions will be installed with the new mirrors the arms finesse will be increased by a factor 3 (F=150). It is also planned to reduce the transmission of the end mirrors down to 3ppm (now T_{WE} = 40ppm and T_{NE} = 10ppm). The coupling factors for the end benches will therefore be reduced by a factor 23 for WE and 5.2 for NE.
From the G factors measured in Virgo one can deduce that the fraction of diffused light (f_{sc}) on the WE bench is as predicted from the expected optics characteristics (f_{sc} =10^{-8}, see [15] section 3.2) while it is a factor 5 to 10 smaller at NE. A factor 2 at most can be attributed to measurement uncertainty. The residual factor 2 to 5 could be attributed to the fact that the second face of the WE mirror is not AR coated and creates secondary beams which might increase the total amount of diffused light. However this hypothesis has not been demonstrated. In order to be conservative, we assume that the diffusion will remain the same for Virgo+MS and only the coupling factor K will be reduced thanks to the increased finesse and smaller end mirrors transmission.

Figure 5.3 shows the impact of diffused light for the NE and WE bench compared to Virgo+MS design sensitivity. Thus, prediction is that the noise should lay a factor 5 to 10 below the design sensitivity. This implies that the NE bench resonance at 18 Hz should be reduced by a factor 2 to 3 (it is now a factor 2 to 3 higher than at WE). This can be achieved by installing a mechanical damper as it is now on WEB. The line at 45 Hz should also be reduced for both benches. This line originates from the fan of the vacuum turbo pump. A seismic isolation of this fan seems feasible and a factor ten reduction of the fan line should not be a problem.

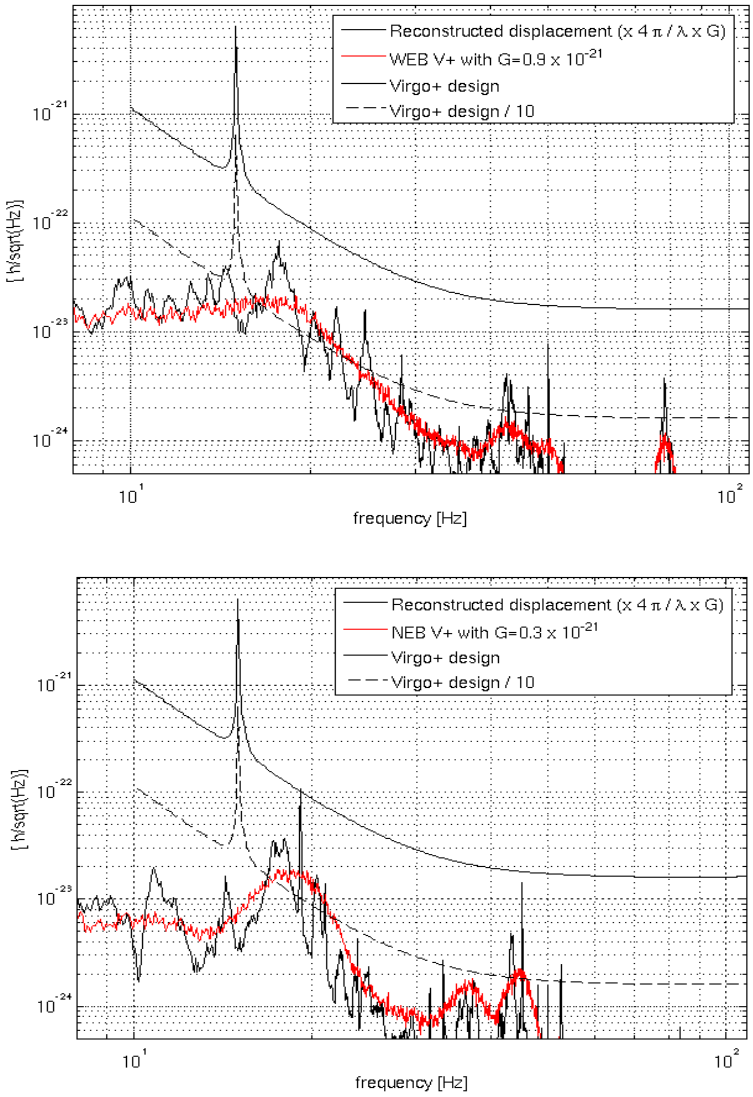

Figure 5.3. Top: Estimation of diffused light noise from WE for Virgo+MS (red) compared to the Virgo+MS design (black) and the design divided by 10 (dashed). The coupling factor has been rescaled with respect to Virgo to account for the new ITF parameters: F=150 and T_{end} =3ppm. Bottom: same for NE.

5.3.2 External detection bench

The case of the external detection bench is a bit more complicated since it receives several beams with different coupling factors. The coupling factor of diffused light of the dark fringe beams before (B1 and B1p) or after OMC (B1s) is:

(Eq. 5.5) $$K_{\mathrm{det},df} = \frac{\lambda}{8FL}\sqrt{\frac{1-C}{2}}$$

where, *1-C* is the contrast defect, before or after the OMC.
While for the B5 beam, or any pick-off beam inside the recycling cavity:

(Eq.5.6) $$K_{\mathrm{det},B5} = \frac{\lambda}{8FL}\sqrt{\frac{R_{BS,AR}}{2}}$$

where, $R_{BS,AR}$ is the reflectivity of the AR coating of the Beam Splitter mirror back face.
The coupling factor of B5 beam scales with the finesse (Eq.5.5) and it should therefore be reduced by a factor 3 for Virgo+MS. The coupling factor of the dark fringe beams (B1p, B1, B1s) scales with *1/F* (see Eq.5.6) but also with the contrast defect, which in turn scales with *F* (from [14]: $1 - C = 2(\Delta P\, F\, /2\pi)^2$). Therefore it is expected that in Virgo+MS all dark fringe beams (B1p, B1 and B1s) will have similar coupling as in Virgo since the mirror defects might be similar.
In the following we discuss individually the contribution for each beam and possible improvements.

- *Diffusion on B1s path*

If, as suspected, the diffusion of B1s presently dominates the noise from the external detection bench this noise would limit the Virgo+MS sensitivity if no action is taken. The diffused light from B1s could be reduced in two ways:

1) A large fraction of B1s is dumped on the suspended bench and the remaining part is still sent to the external bench for monitoring and characterization purposes. If only 10% of B1s is sent to the external bench the impact of diffused light will be reduced by 10 which is enough. This requires to reshuffle the suspended bench and to install on the bench a high power (few Watts) beam dump able to operate under vacuum.

2) The Faraday isolator located after the OMC could be placed before thus filtering the B1s diffused light by the Faraday isolation factor (1000). The impact of diffused light would then be reduced by a factor 30. The suspended bench would need to be reshuffled. One also needs to measure the Faraday back-scattering in order to make sure this will not induce other noise.

These two options have to be evaluated.

- *Diffusion on B1p path*

Since only a small fraction (0.5%) of the dark fringe is sent to B1p photodiodes their induced noise is expected to be a factor 4 below the present total contribution by EDB (see Table 4 in

[15]). Figure 5.4 shows B1p expected noise for Virgo+MS. Assuming the same coupling, B1p noise might lay only a factor 3 below the Virgo+MS design. That could be acceptable if the bench resonances are damped.

- *Diffusion on B1 path*

In Virgo, tapping tests have shown that B1 photodiodes are not the limiting factor on the bench. Indeed their coupling is expected to be a factor 10 below the measured EDB coupling (see Table 4 in [15]). As discussed above, the B1 coupling factor will remain the same for Virgo+MS and this noise will be safely a factor 10 below Virgo+MS design.

- *Diffusion on B5 path*

As discussed above the coupling of B5 diffused light (by the photodiodes) will be reduced by a factor 3 for Virgo+MS. Its expected impact is the same as B1p photodiodes and it is shown in Figure 5.4. Thus, assuming the same coupling, this noise might lay only a factor 3 below the design. That could be acceptable if the bench resonances are damped.

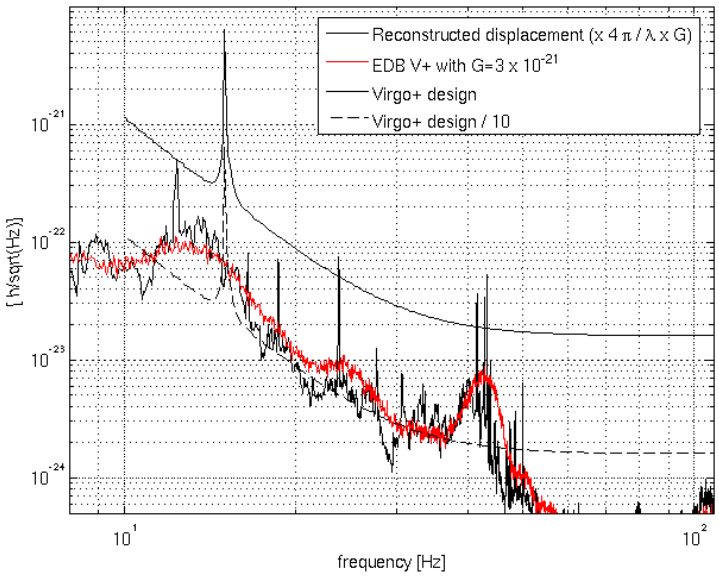

Figure 5.4. Estimation of diffused light noise from EDB for Virgo+MS (red) compared to the design (black) and the design divided by ten (dashed). This noise is dominated by B5 and B1p photodiode contribution. The coupling factor of B5 has been rescaled with respect to Virgo measurement to take into account the new finesse (F=150). It is assumed that some improvements are done on B1s path leading to a reduction of its diffused light noise by at least a factor 10 (see text). B1s noise is therefore expected to be a factor 3 below B5 noise. B1p coupling is expected to remain the same and it could be identical to B5 noise. Thus, shown projected noise is expected to be dominated by diffused light from B1p and B5 beams in similar amount.

5.3.3 External injection bench

For the beams reflected by the interferometer (beam B2) the direct coupling of diffused light was found negligible because is reduced by the gain of the laser frequency stabilization loop (see [14]):

(Eq.5.7) $$K_{inj} = \sqrt{\frac{P_{ref}}{P_{in}}} \frac{f_{rec}}{G_{SSFS}} \nu_{laser} A$$

The last measurement of *G* performed in Virgo only lead to an upper limit (Table 5.1). It is therefore not possible to say if this noise will be a limitation. Figure 5.5 shows the upper limit of EIB diffused light noise assuming the coupling does not change. In any case, since beam jitter is at present limiting the Virgo+ sensitivity, it is planned to improve the support of the injection bench or to place a mechanical dumper for the 18 Hz resonance (see Chapter 8). That should further reduce diffused light if any need.

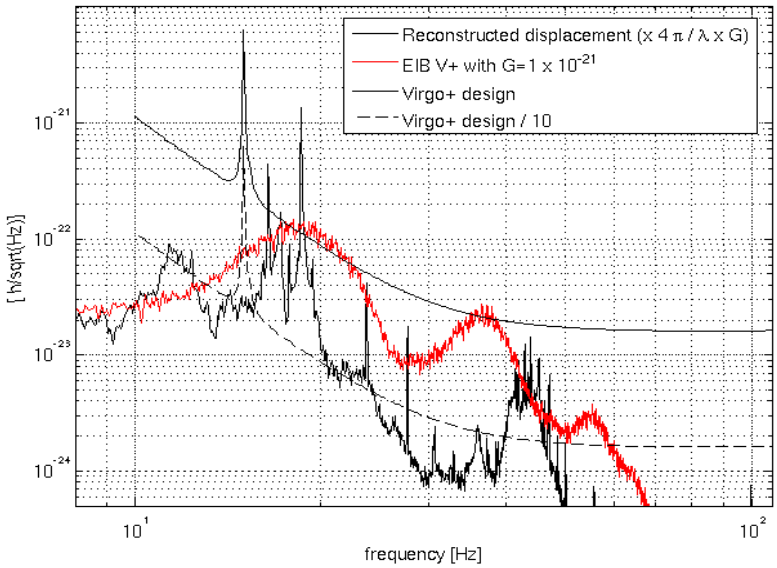

Figure 5.5. Estimate of diffused light noise from EIB for Virgo+MS (red) compared to the design (black) and the design divided by ten (dashed). The projected noise (red) is an upper Limit based on the measured coupling factor upper limit (G≤ 1x10^{-21}).

5.4 Effect of micro-seism in Virgo+MS

In case of increased sea activity (see Figure 5.6) the projected noise contribution from WEB and EDB reaches Virgo+MS design (while NEB is still a factor 3 below design). In this situation an increase of the glitch rate is possible. This environmental condition occurs about 10% of times (see Figure 5.2).

The handle to face this is to reduce further the fraction of diffused light on benches: for WEB it is worth to investigate back-scattering from lens L1 which seems to be the most critical element, if BRDF from L1 turns out to be large, a better coating could be considered. For EDB there is at present no obvious way to further reduce diffused light. We might have a 10% of

dead-time (slightly worsen sensitivity and increased glitch rate) because of diffused light from EDB and WEB.

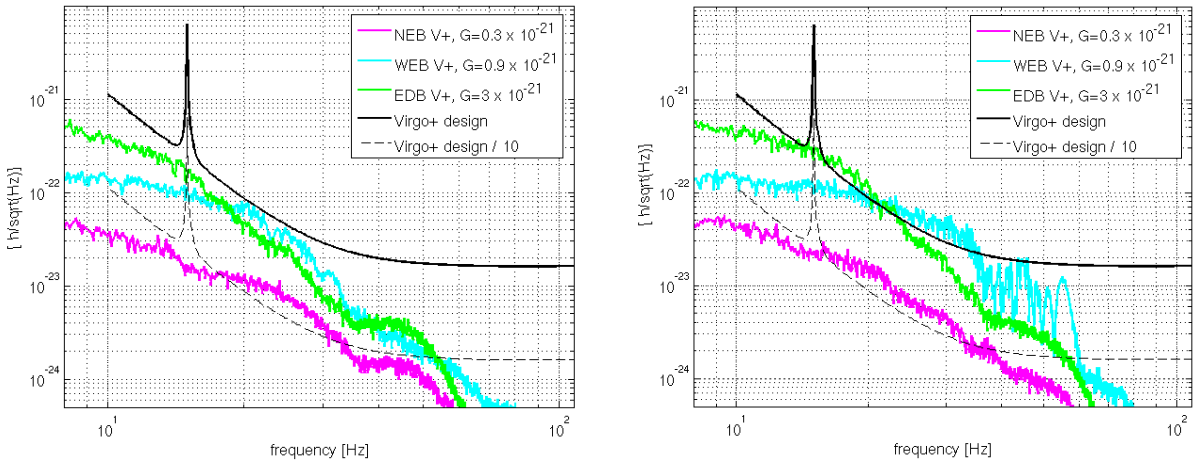

Figure 5.6. Left: Projection of diffused light from external benches in case of medium sea activity (RMS=2microns, 10% of time, see Figure 5.2). Right: case of intense sea activity (RMS=3microns, 3% of time, Figure 5. 2).

5.5 Other back-scattering locations

5.5.1 Detection tower output windows

The beams exiting the detection tower towards the EDB cross two windows: one rectangular window (B1, B1s, and B1p) and one circular window (B5). The rectangular window is probably at present responsible for some diffused light noise observed in the dark fringe (100Hz bump and few more structures between 100 and 150Hz) [16]. Back scattering from the window is probably dominated by diffusion from B1s beam, which is the most intense beam crossing it. This window presently has no Anti Reflective coating. For Virgo+MS the coupling of this noise would be reduced by the Faraday isolation factor (30 times) if this option is adopted, and by the reduced reflectivity of the new window (with an AR coating) and it is expected to become negligible.

The diffusion of B5 beam by the circular window has also to be considered. This window has AR coating. The coupling factor of the output window for B5 is extrapolated in reference [14] to be at least 3 times smaller than the expected coupling for EDB ($G=1x10^{-21}$). Figure 5.7 shows the noise projection. It is worse than in the case of EDB (Figure 5.4) because the tower moves more than the bench (the high frequencies are filtered by the legs for the bench). One can nevertheless expect that the B5 window diffuses much less than assumed here. The environmental noise around 50 Hz and at 100 Hz originate from cooling fans and could also be reduced [17].

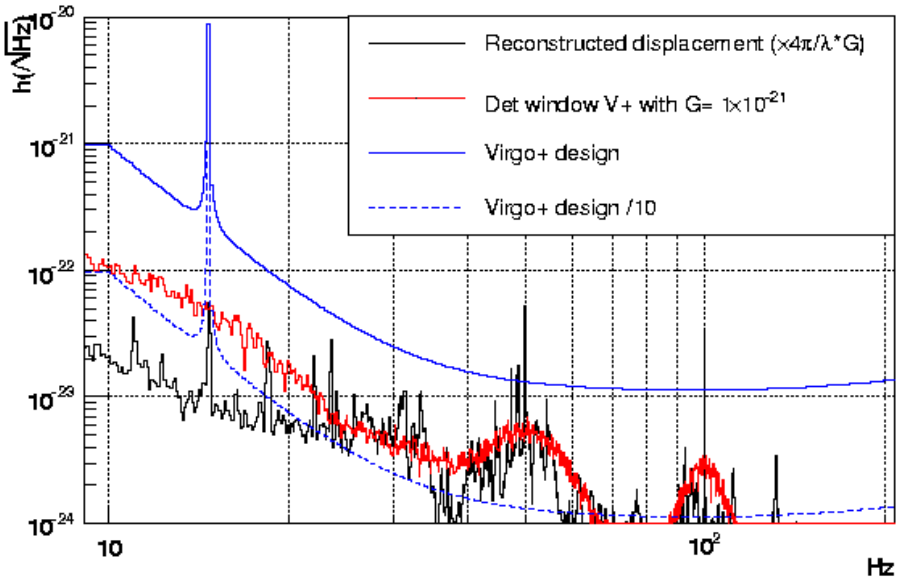

Figure 5.7. Estimation of diffused light noise from the detection output windows for Virgo+MS (red) compared to the Virgo+MS design (black) and the design divided by ten (dashed). It assumed that a FI is installed on B1s, and the residual contribution arises from B5 beam crossing B5 window.

5.5.2 Optical Mounts on Suspended Detection Bench

Resonant modes of the mounts of the M1 and M2 mirrors which are the large mirrors of the SDB telescope spoil the VSR2 sensitivity at 168 and 210 Hz. The suspect is that HO modes are diffused by the aluminum mount surrounding the optics [14, 18]. More rigid mounts have been prepared which have measured modes above 600Hz, and a Q factor of 15-20.

5.5.3 Cryogenic trap

It has been observed during VSR2 an increase of noise in dark fringe (around 60-70Hz and 100-150Hz) corresponding to the refill of the cryo-trap [19, 20]. This noise corresponds to an increased vibration of the LN tank, which has been demonstrated to be caused by the bubbling of the Liquid Nitrogen in the tank.

Since when all suspended baffles in the detection tower have been removed in May 2009 [21, 22] the cryo-trap tank walls are not completely covered for light back reflected from the suspended bench. The bubble noise could in fact be due to diffused light from the tank walls. Possibilities to reduce the noise exist and are being evaluated: (1) identify (measuring BRDF on spares) and substitute critical SDB optics with super-polished ones in order to reduce back-reflection; (2) install new baffles which should be more rigid and not suspended.

Studies are also ongoing (Vacuum group) to understand the mechanism of tank shaking (as for example it has been found that reducing the refill level of the cryo-trap reduced significantly the noise excess, but the reason has not been understood). It is possible that the tank vibration can also be reduced.

6 Actuators noise

This section presents the noise budget for lower stage actuators for Virgo+ with monolithic payloads (Virgo+MS). It refers to document [23] and presentations at the AdV meeting held in Cascina on February 4th, 2010 and at the Commissioning/Detector Meeting on February 8th, 2010.
In Virgo, mirrors actuation along laser beam direction is performed using 6 electromagnetic (magnet-coil) actuators. Two horizontal actuators act on Marionette from the Steering Filter (also known as Filter#7) while 4 actuators act directly on mirror from recoil mass (also known as 'reference' mass). Coils positioned on the RM and Filter#7 legs face magnets which are glued on the mirror and the marionette (also see Section on Magnetic noise).
Starting from position error, the Suspension Control System computes forces using Digital Signal Processors (DSP). In a magnet-coil actuator, force is proportional to the current flowing in the coil. The Coil Driver (CD) is the electronic device that converts the voltage at the output of the Digital to Analog Converter (DAC) into a current flowing into the coil. See schematic draw in Figure 6.1.

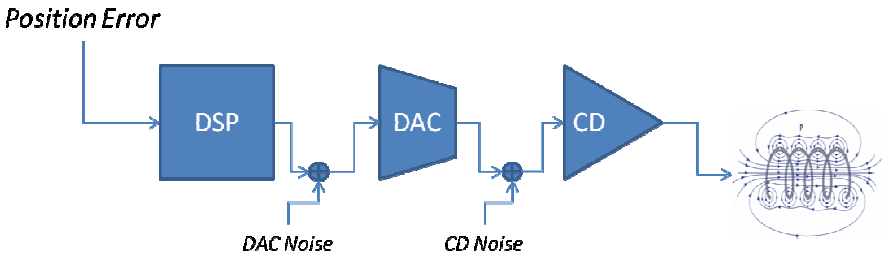

Figure 6.7. Sketch of the Virgo+ RM and F7 control chain.

New Coil Drivers, currently installed at terminal north and west suspensions, have a voltage to current conversion factor that is remotely selectable with a smooth transition from one operation mode to the next one. Five are the available operational modes: HIGHPOWER, used during cavities lock acquisition phase, and LOWNOISE1 to LOWNOISE4 used during linear regime. Changing operating mode we simply change the value of the series resistor. Actual design foresees the possibility to implement shaping filters with order ranging from 0 (no filter) to 5th. Further details on coil drivers and their operational modes can be found in [24, 25 and 26].

1.1 Noise evaluation

The noise of CD is simulated and it is described in [23, 24, 25, and 26]. The DAC noise is measured as described in [27] and [28]. Figure 6.2 describes CD noise and DAC noise for different operating modes. Noise reduces by about a factor 10 going from LOWNOISE1 to LOWNOISE4. Note that the LOWNOISE4 mode means using a x4 series resistor thus reducing the CD output current, and consequently the actuation force, by a factor four.

The corresponding displacement noise of mirrors is obtained by multiplying the DAQ plus CD noise in Figure 6.2 by the RM-Mirror or the Filter7-marionette mechanical transfer functions here below, which include the DC coil actuation factor:

- acting with 1 RM coil: $|H_{RM}(f > f_{0)}| \cong 5.5\times10^{-6}\frac{f_0^{\,2}}{f} \cong \frac{2\times10^{-6}}{f^2} m/A$
- acting with 1 F7 horizontal coil: $|H_M(f > f_{0)}| \cong 7\times10^{-6}\frac{f_1^{\,2} f_2^{\,2}}{f^4} \cong \frac{1.4\times10^{-6}}{f4} m/A$

Finally, the noise projection in units of strain is obtained by multiplying by the meters to strain coefficient, which for arm mirrors is 1/L, L = 3000m, and summing incoherently over the number of actuating coils.

Figure 6.3 shows the noise projections in units of strain for the four arm mirrors and marionettes for the actuators configuration in use during VSR2. The detail of the calculation, in the form of printout of the *matlab* script, is provided in document [23].

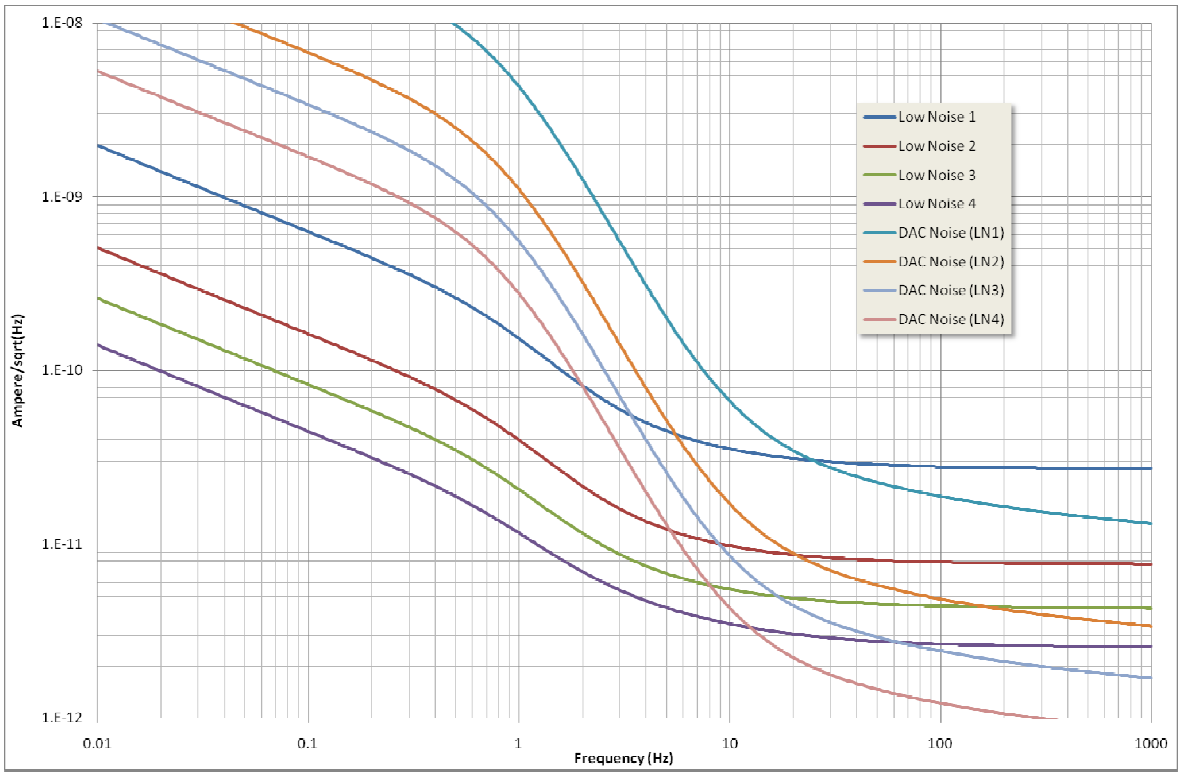

Figure 6.2. Output Noise: Coil Driver and DAC Contribution

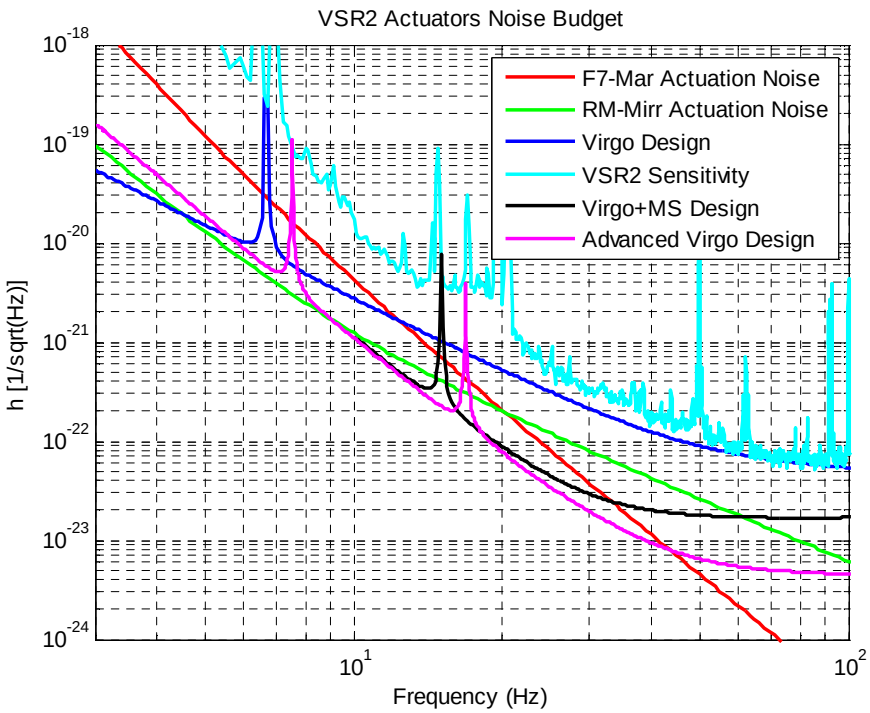

Figure 6.3. VSR2 Actuators Noise Budget (Long Arms only). The VSR2 actuation scheme was consisted of: (i) new coil drivers in LOWNOISE1 mode acting on two coils at NE and WE; (ii) NI and WI mirrors, due to the extremely large value used for series resistors (6 kOhm), gave a negligible contribution to long arms actuator noise;(iii) Filter #7-Marionette actuators used the old type CD with a first order shaping filter.

1.2 Signal dynamic and V+MS projection

Adding a series resistor to the coil we can reduce the noise equivalent displacement, but of course in this way we also limit the maximum displacement we can achieve. A correct evaluation of required dynamical range is therefore important for selecting a proper operational mode.

During VSR2 we used only a small fraction of available dynamical range. As described in [23], the full dynamical range (LOWNOISE1) was needed just for a small fraction (less than 5%) of time, in correspondence of bad weather conditions. In this condition the sensitivity below 100Hz was typically limited by other independent instrumental noises, mainly diffused light (see Sec. on diffused light). As demonstrated in [23], during VSR2 the RM–mirror actuators could have been operated in LOWNOISE2 mode (4x series resistor) for about 95% of science mode time and in LOWNOISE3 mode (8x series resistor) for more than 80% of science mode time; while the F7-marionette actuators could have been operated for 99% of science mode time inserting a 5x series resistor.

After monolithic payloads installation, thermal noise contribution to Virgo sensitivity will drop down and a reduction by a factor of about 5 of actuation noise is needed. Meeting requirement for actuation noise is possible using the LOWNOISE2 mode at reference mass level and adding a 5x series resistor to marionette actuators. With respect to VSR2 configuration the actuators

noise will thus reduce by a factor 5 for the marionette actuators and by a factor 5 to 5.5 for the mirror actuators. Figure 6.4 shows the projected noise for RM and F7 actuators in the mentioned configuration.

Only the noise contribution of arm mirrors is shown in Figure 6.4. The noise contribution from BS and PR mirrors actuators is expected to be negligible with respect to other mirrors, and this comes from the following considerations. For the BS, we expect the noise to be reduced by the arm finesse factor (F = 150 for Virgo+MS) and thus to be confidently below the arms actuation noise[1]. For the PR, an experiment (eLog 22334) demonstrated that it can be considered negligible with respect to arms actuation noise.

To be noticed that further improvements are possible implementing second order filter at Filter#7-Marionette level[2] and switching to LOWNOISE3 mode at reference mass – marionette level. Furthermore acting on more coils (at present we use only 2 of the 4 coils available) and/or more mirrors (at present we act only on end mirrors and we do not use input mirrors for cavities longitudinal lock) [3].

The necessary hardware installations for Virgo+MS are described in the change request document [29].

[1] The CD used for RM actuation of the BS have an actuation factor (α = 27.4 μm/A) which is about 4 times larger than that of other mirrors CD (α = 7.5 μm/A). This factor 4 is partially compensated by (i) a factor sqrt(2) coming from the fact that the actuating force on BS is split over 4 instead of 2 actuators, and (ii) another factor sqrt(2) coming from the fact that on BS actuation force is exerted at 45 degrees with respect to mirror displacement.

[2] The actuation force at low frequency is mostly exerted at F7-Marionette level. A higher order shaping filter on F7-MA CD would allow increasing the dynamical range at low frequency without changing the contribution of CD noise above 10Hz.

[3] If for example we act of 4 instead of two coils, the noise supposed uncorrelated (generally true) sums in quadrature and thus increases as a factor sqrt(2). At the same time, the force is split in two and so is the current, the series resistor can thus be doubled reducing the noise by a factor 2. So doubling the number of actuating points reduces the noise by a factor sqrt(2).

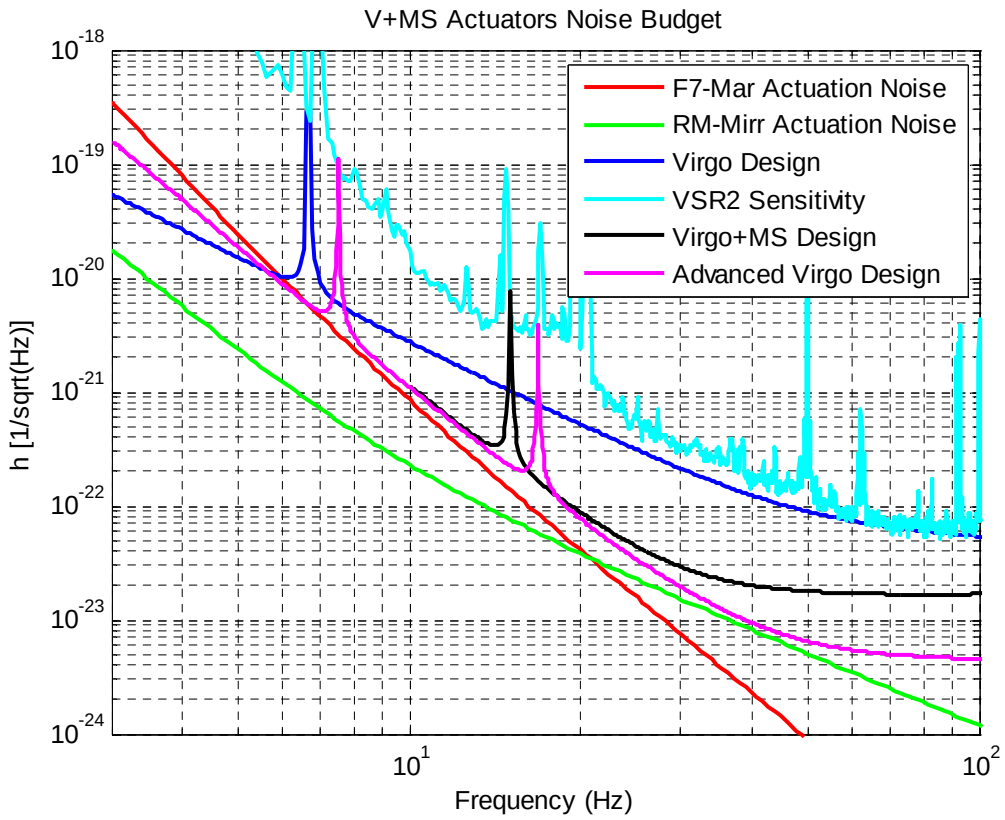

Figure 6.4. Virgo+ Monolithic Payloads Actuators Noise (Long Arms only).

7 Magnetic noise

7.1 Introduction

For controlling the length of the Virgo interferometer, small magnets are glued to all mirrors. These magnets can influence the sensitivity at low frequency by two different mechanisms: First of all, a movement of the magnets can induce eddy currents in the reference mass, which leads to a viscous damping of the main pendulum modes of the mirrors. This effect is already included in the model of the thermal noise (see [3]) and will not be considered here. The second effect of the magnets is that they can couple environmental magnetic fields to a displacement of the mirrors, which is the focus of this chapter.
This chapter will first discuss the various magnetic noise projections, which try to predict to which amount magnetic noise is contributing the sensitivity. The rest of the chapter will discuss how this contribution can be reduced in 2 different ways, first by reducing the coupling between the magnetic field and the mirrors, and secondly by identifying and curing sources of magnetic noise.

7.2 Magnetic noise projections

To get an estimate of how much magnetic noise contributes to the sensitivity, several dedicated experiments have been performed. More details about these measurements will be described in a future Virgo note; only the final results will be presented here.

7.2.1 Far-field injections

In Virgo a number of very sensitive magnetometers, which are positioned close to the mirrors, are used to probe the background magnetic noise. In a simplified view, one could assume that all the magnetic noise sources are located far away from the mirrors, so that both the magnetometers and the mirrors see more or less the same field. If a transfer-function is known between the signal of the magnetometers and the output of the interferometer, a linear noise projection can be made.
This transfer-function can be measured by injecting strong sinusoidal magnetic fields at a number of fixed frequencies and measuring simultaneously the result in the magnetometers and in the output of the interferometer.
For this purpose, a large coil was built that has been optimized for the injecting the strongest field around 100 Hz. Injections were performed with the coil in several locations in the various buildings, and with the axis of the coil pointed along all 3 directions. To fulfill the far-field condition, the coil is always placed as far away as possible, but this is usually limited by the building to a distance of around 15 meter. To retrieve the injected signal from the output of the interferometer, integration times of up to 10 minutes were used.

A magnetic noise projection can finally be calculated by interpolating the obtained transfer-function and multiplying it with the spectrum of the magnetic noise measured in quiet conditions. The resulting projection for the various buildings is shown in Figure 7.1. Note that these projections have a pretty large uncertainty. Similar measurements with the coil located in other positions, showed that the results can vary by as much as a factor 3. One source of errors is the fact that magnetic fields are vector fields, which have to be simplified to scalar fields to make the projections. It has to be stressed, finally, that these projections are only valid if all the sources were located far away, which is not completely true in reality. Some sources will be closer to the mirrors and will thus be underestimated. Other sources might be further from the mirrors but close to the magnetometers, which might lead to overestimation. The main conclusion of the far-field injections is that the contribution of the Central Building is the highest and probably comes closest to the sensitivity between 20 and 30 Hz.

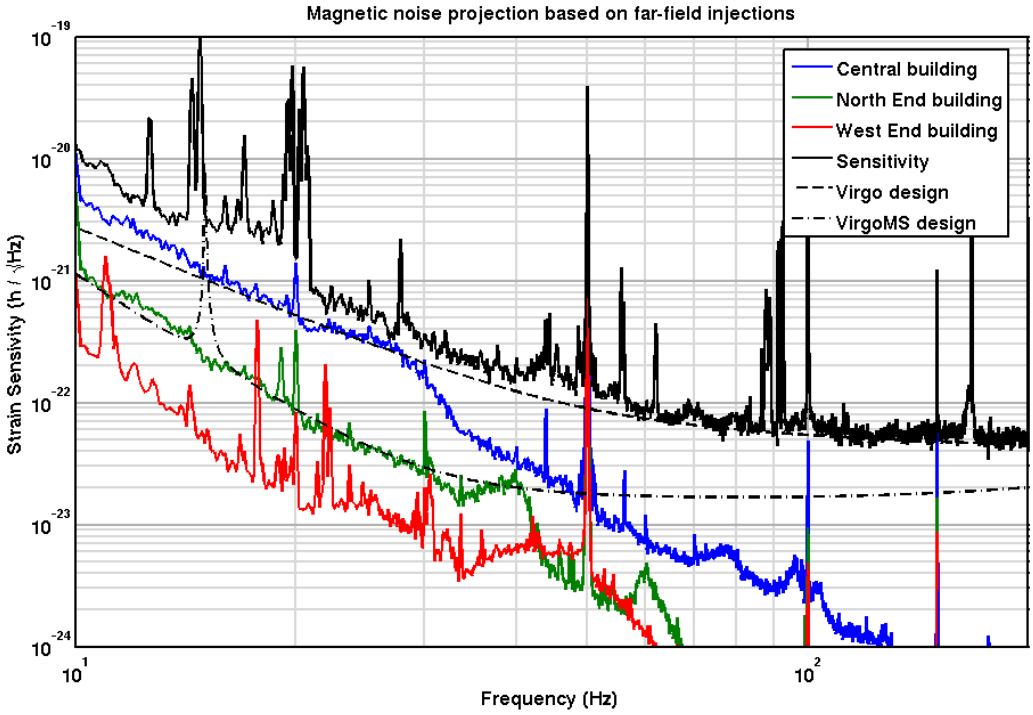

Figure 7.1. Magnetic noise projection for the different buildings obtained by injections lines from the far-field.

7.2.2 Near-field injections

The measurements described in the previous section give an idea about the contribution of all the mirrors in a single building. To determine the contribution of individual mirrors, magnetic noise has also been injected from the near-field, by placing a small coil inside the ovens, as close as possible to the mirrors.

The results can be compared to the transfer-functions obtained by the far-field injections by using a dipole model for the field injected by the coil. The results of the near- and far-field

methods agree to within an order of magnitude, but probably large errors are made in the model.

The main goal of these measurements is however not to obtain a transfer-function, but to make a qualitative comparison of the contribution of the individual mirrors, which is shown in Figure 7.2. It is clearly seen that the contribution of the beam-splitter mirror dominates when the magnetic field is applied along one particular direction. This can be explained by the fact that a field in this orientation induces a rotation around Y, which can couple to the longitudinal degrees of freedom due to a very large (~1 cm) mis-centering of the beam on the beam-splitter along X. In theory, the effect of a movement of the beam-splitter should be a factor 50 less than that of the input-mirrors, but this is compensated by the fact that the beam-splitter is 4 times lighter, and by the fact that it has stronger magnets.

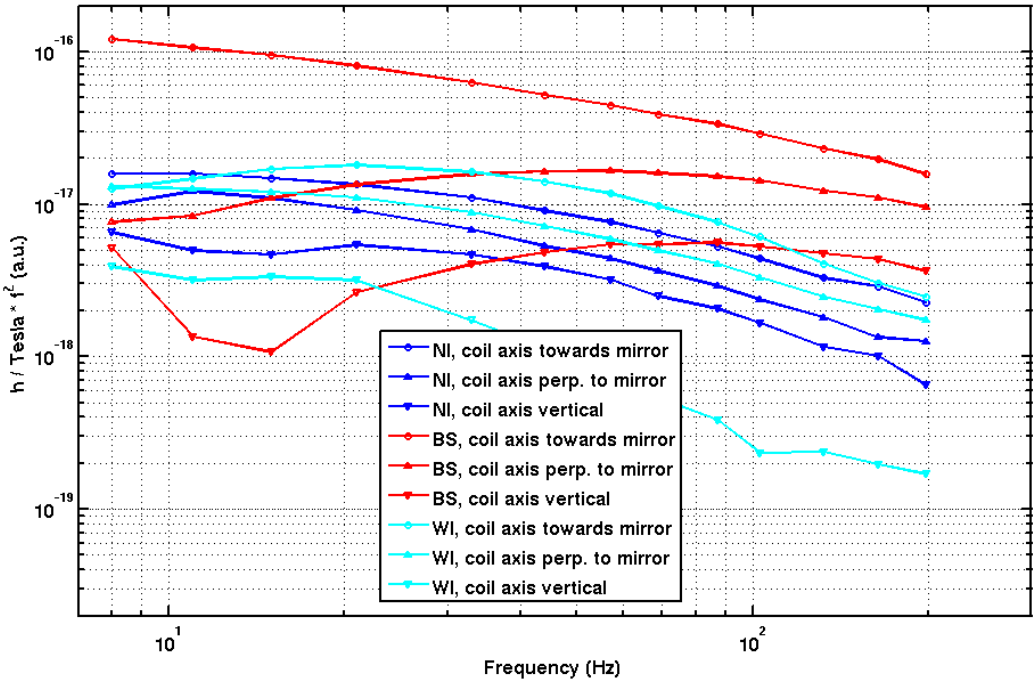

Figure 7.2. Transfer function of gravitational strain per Tesla, for the North Input (NI), West Input (WI) and Beam-Splitter (BS) mirrors. All curves have been multiplied by f ^{2} to remove the response of the mirror pendulum. The remaining frequency dependence is probably due to magnetic shielding effects.

7.2.3 Noise projection using long coherence

A third method to make a magnetic noise projection does not use any injections, but uses only the coherence between the magnetometers and the dark fringe averaged over very long periods. The spectrum of the projected noise is then calculated as the square root of the coherence multiplied by the actual sensitivity. Figure 7.3 shows the noise projection calculated using this method for all the buildings. For this measurement 7 hours of data was used, which allowed for

5000 averages. In this way, it was possible to retrieve noise sources that are a factor 30 below the sensitivity. The result shows again that the contribution of the central building is dominating, with a bump between 20 and 30 Hz about a factor 5 below the sensitivity. Also the sidebands around the 50 and 100 Hz lines are contributing a bit, as are a few lines which are known to be caused by fans. At other frequencies, the noise is not contributing significantly to the sensitivity.

This method seems to give more accurate projections than those described in the previous two sections. It should properly predict all the noise that is seen by both the interferometer and the magnetometers. The only thing not accounted for by this projection would be noise sources that are really close to the mirrors, but too far away from the magnetometers to be seen above other noises. To exclude this possibility, similar measurements were performed with a portable probe placed inside the ovens, very close to the mirrors, which showed similar results.

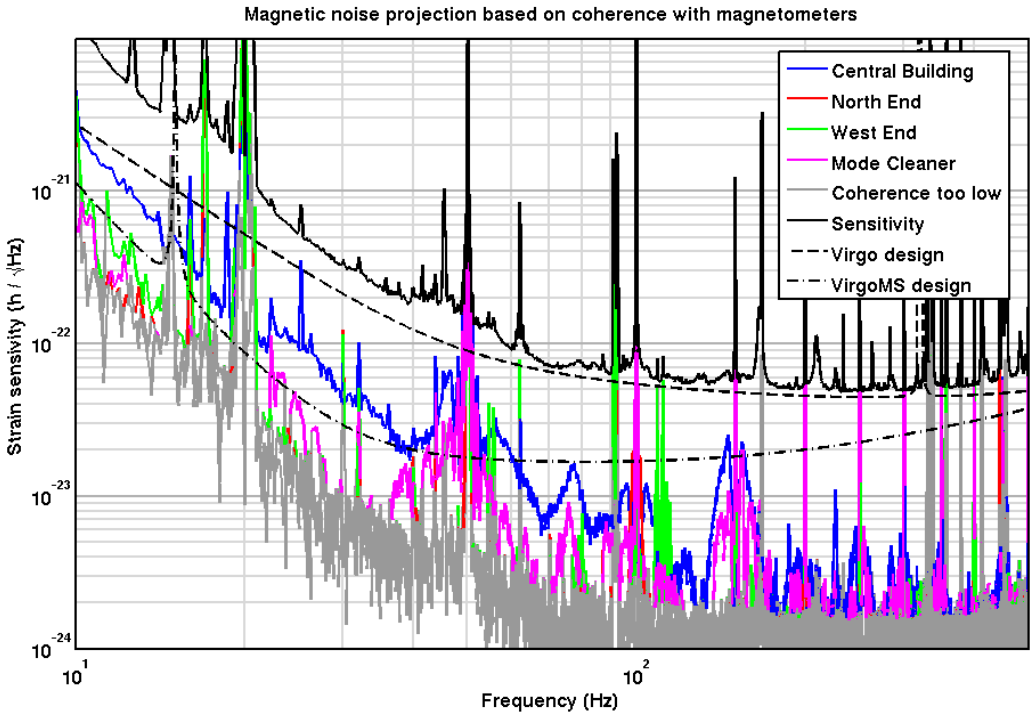

Figure 7.3. Magnetic noise projection based on long coherence with the magnetometers.

7.3 Reducing the coupling between mirror and magnetic field

7.3.1 Magnet replacement

One obvious way to reduce the coupling of magnetic fields to mirror motion is the reduction of the strength of the magnets. Since the magnets are used for the control of the mirrors, they must

be able to provide a certain force. In principle, the loss of magnet strength can be compensated by an increase of current sent to the coils, but obviously there are practical limits to this current. In the past, the strength of the magnets glued to the input- and end-mirrors has already been reduced by a factor 5.5.

Apart from the 4 magnets glued to the back of the mirror for longitudinal and alignment control, there are also 2 mirrors glued to the side, intended for damping a possible excitation of the pendulum mode in the X-direction. Injections from the near-field showed that one mirror that still had these magnets had a considerable larger coupling factor than one where the magnets had detached [30]. A strategy has been developed to damp these X-oscillations with the help of the 4 magnets on the back only. The lateral magnets were thus not needed anymore and have been removed from all the mirrors.

Recent near-field injections showed that the contribution of the beam-splitter is now dominating. In theory, the gravitational channel is less sensitive to disturbances acting on the BS mirror than to those acting on the input or end-mirrors by a factor related to the finesse of the arm-cavities. This is however compensated by the fact that the BS is 4 times lighter (so it will have 4 times the displacement for the same force) and by the fact that it still had the old, strong magnets. Moreover, it is possible that these magnets are oriented in the wrong, parallel orientation and that the lateral magnets are still present. Finally, the beam has a large offset of the beam along X, which means that it can couple via a rotation around Y. The measurements show indeed that it has one very sensitive direction.

To reduce the effect of the beam-splitter, it is therefore foreseen to reduce the strength of its magnets at the time of the Virgo+MS shutdown. The new magnets should be installed with the correct orientation and possible lateral magnets should be removed.

7.3.2 Reference mass

Measurements on a spare aluminum reference-mass showed that eddy currents induced in the material will locally disturb the magnetic field, similar to how a lightning rod disturbs an electric field [31]. This means that even homogeneous magnetic fields will cause a gradient exactly at the position of the magnets, which leads to an enhanced coupling to magnetic fields. Because eddy current will also cause viscous damping of the pendulum mode, it was already decided to design the new reference mass for the monolithic suspensions largely out of dielectric material. This change in design will thus also reduce the coupling of environmental magnetic fields. How much would be gained by this change is hard to estimate, this would require a full 3-D electro-magnetic modeling of the reference mass.

7.4 Sources of magnetic noise

Another strategy to reduce the effect of magnetic noise on the sensitivity is to hunt for the sources of the noise and cure them. Already more than 2 years ago, it was found that big bumps around 100 Hz were caused by power-supplies of the local-control lights located inside the

ovens [32]. This was solved by simply moving the power-supplies further away. This section will describe some sources that have been found more recently.

7.4.1 Electronic racks

Some possible sources of magnetic noise close to the towers are the racks of the suspension electronics and the vacuum system. Evidence was found that some of them contain noisy power supplies. Ideally, these racks should be displaced as far away from the towers, but this will not be possible on the short term. More work is needed to see if any noisy components can be replaced or shielded.

7.4.2 Mode cleaner air-conditioning

Already last year, it was discovered that some very strong sidebands around the 50 Hz line are caused by the heating of the Mode-Cleaner building [33]. This heater consists of an electrical load of around 10 kW, which is pulse-width-modulated at a few Hz. As a temporary solution, the controller has been modified to lower the pulse-width-modulation frequency. This effectively brings the sidebands closer to the 50 Hz line so that they are hardly visible in the sensitivity. A more permanent solution would require the replacement of the heater or its switch.

Analysis by the burst group found some glitches in the dark fringe once every 20 minutes, which are also seen in the magnetometers of the Mode Cleaner building. The source of this problem was later found to be the chiller of the cold-water circuit, which produces a glitch when it is switched on [34]. It should be possible to fix this problem with some simple electrical filter.

The exact path along which both the heater and the chiller can couple to the interferometer is not known, but since both events are clearly seen in the power line of the Central Building, it is believed that this disturbances are radiated there as magnetic noise and picked up by the mirrors. Solving this kind of coupling via the power-line between buildings might require extensive modifications of the power distribution network.

7.4.3 UPS noise

Recent tests showed that an important part of the magnetic background noise might be caused by the uninterruptible power supply (UPS) of the central building [35]. Figure 7.4 shows that when the UPS is switched off, the level of the magnetic background noise decreases by almost an order of magnitude over a wide bandwidth. The reason why the UPS is so noisy is still being studied, but is hoped that it might be solved by some modification of the machine, probably in close collaboration with its manufacturer.

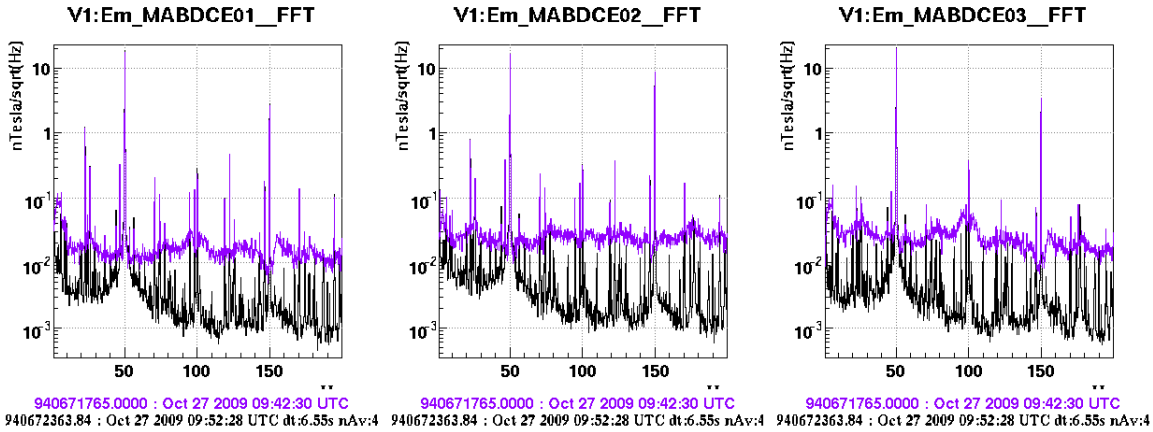

Figure 7.4. Magnetic noise measured by the magnetometers of the central building when running on UPS power (purple) and when connected directly to the grid (black).

7.5 Conclusion

The most accurate noise projections, based on long averaged coherences, show that magnetic noise is currently not limiting the sensitivity. Only around 25 Hz, around the 50 and 100 Hz lines it is contributing a bit. This predicted level is, however, at the level of the design curve for Virgo+MS, so an improvement by about an order of magnitude is required to make the contribution of magnetic noise negligible with respect to the fundamental noises.

For Virgo+ with monolithic suspensions, a reduction of the coupling is expected due to the change of the magnets of the beam-splitter. This should bring its contribution to below that of the two input mirrors, which might reduce the contribution of the central building by a bit more than a factor of 2. A further reduction of the coupling is expected from the change from an aluminum reference mass to a dielectric one. Unfortunately, it is not possible to exactly quantify these improvements.

Further reduction of the magnetic noise must be achieved by finding and curing the sources of the noise. A large improvement is expected if the noise of the uninterruptible power supply of the central building can be made less noisy.

8 Noise from Input Beam Jitter

The residual noise associated to the jitter of the input beam has been measured during VSR2 [36] and shown in Figure 8.1. Above 10Hz beam jitter is mainly associated to the seismic motion of the External Injection Bench (EIB). The large noise structure around 40Hz visible in Figure 8.1 is associated to the first vertical mode of the bench on its supporting legs [37], while the largest peaks above 200Hz are associated to mechanical resonances of optical mounts which we suspect to all be on EIB [38,39]. The noise is going to limit Virgo+MS sensitivity. In order to be compliant with Virgo+MS design, assuming a factor 10 safe margin, the bench top motion needs to be reduced by a factor of about 50 at 40Hz, and by a factor 10 above 200Hz with respect to present motion. In order to reduce the noise of B2 quadrant photodiodes which could be used for AA (see Chapter 3) it is also necessary a reduction of a factor of 30 of the EIB motion below 30Hz. The EIB motion below 30Hz is mainly associated to horizontal modes (around 16Hz) of the bench on its supporting legs [37].

We have evaluated different strategies for reducing the bench motion. The damping of the 40Hz mode using a resonance damper (of the type on the one installed on NEB and WEB [40]) has been excluded: because of the characteristics of the EIB vertical mode (quite broad) the energy dissipation by such a system would be small and by far insufficient. The strategy of increasing the stiffness of the "bench plus legs" system with the consequence of moving the vertical mode frequency to higher values has also been investigated. Attempts and test performed either on EIB [41], or with the similar bench in Optics Lab [42] proved difficult to increase the system rigidity and the modes frequency by more that 20% with simple interventions. The system rigidity would be ultimately limited by the resonant modes of the bench itself which are presumably around 150Hz. However, the bench stiffening strategy seems not useful, since the high-frequency bench motion would increase as well as the contribution of noise from optical mounts, which is large at first place.

The only effective strategy seems that of improving the isolation of the bench from ground adding an isolation stage with low frequency cut-off. The requirements of such isolation system have been defined. The system must have a similar isolation performance along the vertical and horizontal directions. A cut-off frequency of less than 3Hz seems necessary in order to guarantee the isolation requested. We have to avoid amplifying too much the bench motion at low frequency (< 3Hz): the ground seism at low frequency is subject to large daily and seasonal variations (a factor 10 is typical) because of the site anthropogenic noise and sea + wind activity. An amplification of present maximum bench motion of more than a factor 5 might cause up-conversion noise through diffused light (see Chapter 5). Thus, a Q factor of the isolating system at its resonance frequency of less than 5 is advisable. The EIB is the external position reference for the whole ITF. Thus it is necessary that the system has small hysteresis, and in case of solicitation it can recover the initial bench position within less than 10 microns. It is also necessary that drift with time of the bench because of the added isolation system (due for ex. to internal creeps) is small in order to permit the Beam Monitoring System control to compensate for this drift keeping the input beam alignment. A drift rate of the order of a few microns per month (after allowing for initial settling) is acceptable.

One possible solution (the active isolation system STACIS by TMC) has been identified and it is presently being evaluated by the Nikhef group [43, 44]. Another possible solution is that of damped spring supports (passive damping). This configuration is also being studied by Nikhef.
The coupling of beam jitter noise to dark fringe can change with the new ITF optical parameters. This information shall be extracted from a simulation model of the beam jitter coupling in the ITF that is currently being studied by the Napoli and EGO optics group and shall be ready soon.

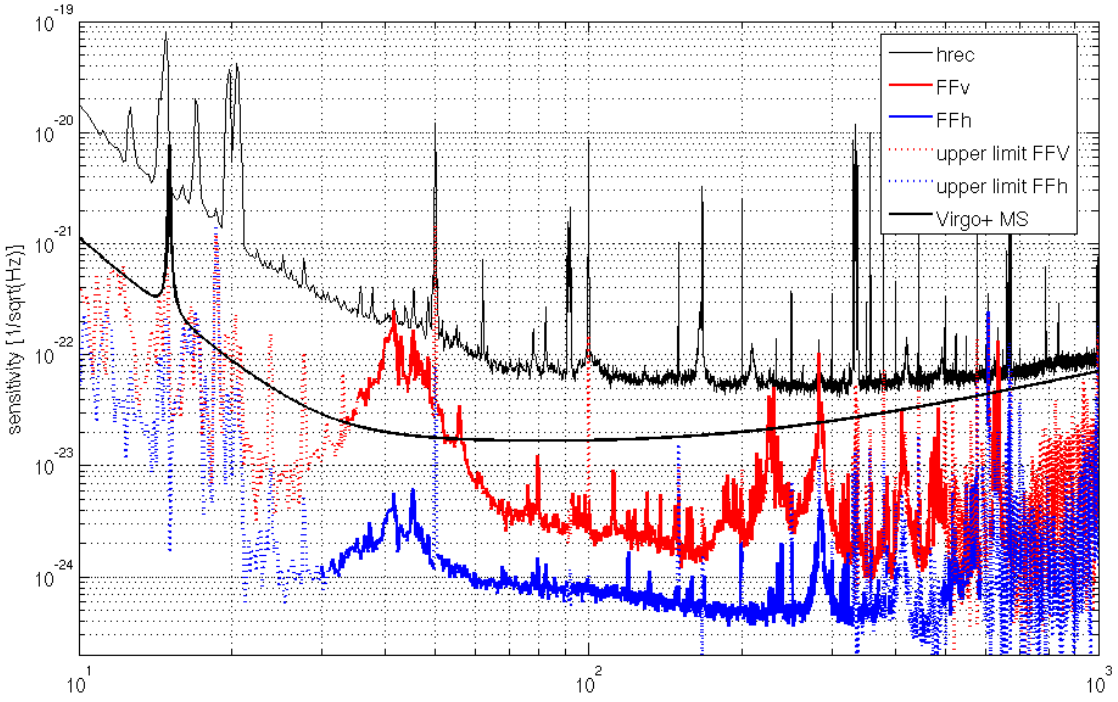

Figure 8.1. Contribution of jitter noise of the input beam measured along the vertical direction (red) and horizontal direction (blue) compared to Virgo+MS design. The noise around 40Hz is associated to the vertical resonance of the EIB; structures between 200 and 500Hz are associated to mechanical mounts of the optics of BMS; between 70Hz and 200Hz the measurement is likely limited by the noise of the BMS quadrants. The horizontal jitter noise is smaller or less coupled to the sensitivity. This has not been yet understood.

9 Frequency noise

In Virgo the Second Stage of Frequency Stabilization (SSFS) uses B5_ACp error signal. The laser frequency noise is well cancelled by the SSFS and its impact is negligible in Virgo (see Figure 9.1: dark blue curve). However, the shot noise of B5 is re-introduced as frequency noise by the SSFS and this noise limits the Virgo sensitivity above few 100 Hz (see Figure 9.1: light blue line). In this Chapter we extrapolate this control noise from Virgo+ to Virgo+MS configuration. More details can be found in reference [45].

9.1 Frequency noise and B5

A frequency noise δν at the input of the ITF is seen on B5 photodiode as:

(9.1) $$B5\_ACp = K\delta\nu \frac{1}{\sqrt{1+(f/f_{rec})^2}}$$

Where the DC optical gain, K, is expected to vary with the input power P_0, the Beam Splitter reflectivity R_{BS}, the recycling gains of the carrier G_{rec} and the sidebands G_{SB}, the finesse F:

(9.2) $$K \propto P_0 R_{BS} \sqrt{G_{rec} G_{SB}} F$$

It has been measured in Virgo for P_0=8Watts, G_{rec}=43, G_{SB}=20: K=1.4x10^{-3} W/Hz (from [46]). It is extrapolated for the present (Virgo+) optical parameters (P_0=17 Watts, G_{rec}=43, G_{SB}=30): K=3.8x10^{-3} W/Hz and the same way for Virgo+MS parameters (P_0=25 Watts, G_{rec}=20, G_{SB}=30, this last parameter is assumed to remain the same as now): K=1.1x10^{-2} W/Hz.
The B5 shot noise on B5_ACp is given by:

(9.3) $$B5\_ACp\_sn = \sqrt{2h\nu P_{B5}}$$

Where, the power of B5 beam is $P_{B5}=P_0 G_{rec} R_{BS} R_{BSAR}$, R_{BSAR} is the reflectivity of the second face of the BS mirror, which is 550ppm.

9.2 Coupling of frequency noise

The frequency noise δν couples to the dark fringe through:

(9.4) $$h(f) = CMRF(f)\frac{\delta\nu}{\nu}$$

where *CMRF(f)* is the common mode rejection factor given by the arms asymmetries (mainly the finesse and the losses).

9.2.1 Losses asymmetry

For a losses asymmetry ΔP the CMRF is given by:

(9.5) $$CMRF(f) = \frac{F}{2\pi}\Delta P \frac{1+if/f_{cav}}{1+if/f_{rec}} \cdot \frac{f_{cav}}{f_{rec}}$$

where, f_{cav} is the pole of the Fabry-Perot cavities (f_{cav}=c/(4LF), that is 500 Hz in Virgo, 167 Hz in Virgo+MS) and f_{rec} is the pole of the double cavity (around 8 Hz in Virgo and Virgo+MS). In Virgo the losses asymmetry have varied from 50 ppm to 170 ppm (now). The reason of this change has not been understood. It could be related to a change in the alignment working point. The Virgo+MS mirrors have the same quality of polishing as Virgo mirrors; we therefore assume that the losses asymmetry will remain the same. Combining Equations (9.1), (9.2), (9.3), (9.4) and (9.5) and using Virgo+MS parameters it is possible to project the impact of B5 shot noise on the new sensitivity. The result is shown in Fig 9.1 (left, red curve).

9.2.2 Finesse asymmetry

For a finesse asymmetry ΔF the *CMRF* is given by:

(9.6) $$CMRF(f) = \frac{\Delta F}{F}\frac{1}{1+if/f_{rec}}$$

In Virgo the finesse asymmetry varies (and can be tuned) thanks to the so-called etalon effect (a variation of the reflectivity due to a change of thickness of the substrate when its temperature changes) in the input mirrors:

(9.7) $$\frac{\Delta F_{\max}}{F} = \pm 2\sqrt{R_{AR}}$$

where R_{AR} is the reflectivity of the AR face of the input mirrors (R_{AR}=150ppm in Virgo). In practice the etalon effect is tuned by varying the power of the TCS laser incident on the input mirrors, thus changing the temperature of the substrate. The same technique could be used for Virgo+. For Virgo+MS the input mirrors have been coated at the same time and have equal reflectivity, therefore the finesse asymmetry will be entirely due to the etalon effect. The AR coating of the first Virgo+MS input mirror is R_{AR} ~300ppm. The second mirror has been coated with a very small AR, therefore one can expect to be able to tune the finesse asymmetry from 0 to +/-3.5%. Combining Equations (9.1), (9.2), (9.3), (9.4) and (9.6) and using Virgo+MS parameters it is possible to project the impact of B5 shot noise on the Virgo+MS sensitivity for a finesse asymmetry of 3.5%. The result is shown in Fig 9.1 (left, blue curve).

9.3 Frequency noise projection for Virgo+MS

The contribution of frequency noise due to finesse asymmetry and to losses asymmetry is shown in Fig 9.1(left) for Virgo+MS. The noise due to losses asymmetry will limit the Virgo+MS sensitivity above typically 60 Hz (h will increase by about 10%) if the etalon effect is not used. If the etalon effect is used (as now in Virgo) the finesse asymmetry can be used in

order to compensate a bit the losses asymmetry below 100 Hz. This is shown in Fig 9.1(right, blue curve). The Virgo+MS sensitivity will nevertheless be limited by frequency noise above typically 200 Hz. The uncertainty in this noise projection is the losses asymmetry which is assumed to remain as in Virgo+. As shown by Equation (9.5) the frequency noise will scale with the losses asymmetry.

It could be envisaged to use B2 instead of B5 as error signal for the SSFS but this was investigated in VIR-NOT-OCA-1390-227 and was not found to give better performances. The only possibility to reduce the impact of this noise seems to be the alignment working point but the handle is probably small. It should be also underlined that the mismatching of the beam to the cavities also introduces losses asymmetry if the arms are not symmetric. The matching of the input beam to the Fabry-Perot cavities should therefore be optimized.

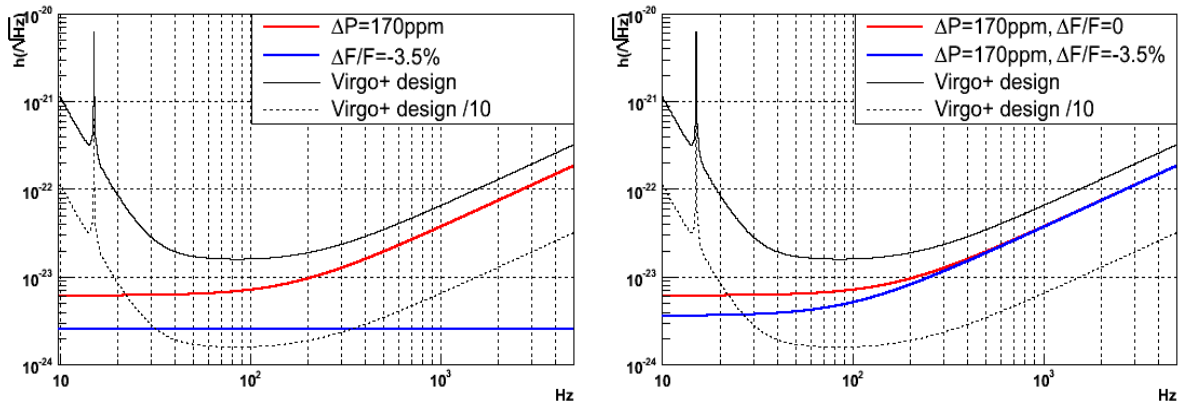

Fig 9.1. Projection of frequency noise due to B5 shot noise for losses asymmetry of 170ppm (red) and finesse asymmetry of 3.5% (blue). On the right the effect of losses asymmetry and of finesse asymmetry are combined into the blue curve.

10 Phase noise

The phase noise arise in the demodulation process and is due to phase noise on the 6 MHz signal itself and phase noise introduced by the LO or demodulation boards. This phase noise is typically 0.2μrad/Hz. It couples to B1_ACp proportionally to the RMS of B1_ACq [45]. Since B1_ACq is used for the MICH control its RMS is very small. The present projection is shown in Figure 1-1 (purple line) and is indeed negligible. If the control scheme is the same for Virgo+MS this noise will remain negligible. In case B1_ACq is not used anymore for MICH control it can anyway be kept small enough by properly tuning the alignment and locking working points. This noise is therefore considered to remain negligible for Virgo+MS.

11 Conclusions

The projected noise contributions described in the previous Chapters are superposed in Figure 11.1 and compared to the Virgo+MS design curve described in [3] which accounts for fundamental noises. The incoherent sum of the noises is shown in Figure 11.2. The shown noises represent the situation if no major action is made in order to reduce magnetic noise and input jitter noise which would dominate below 100Hz. For the TCS noise, the shown projection uses a conservative noise case which corresponds to the optimal compensation (Section 4.2.2). At high frequency B5 shot noise is the limiting contribution (Chapter 9). Figure 11.2 also shows the incremental contribution due to TCS, beam jitter and magnetic noises.

A reduction of magnetic noise and beam jitter noise is necessary and possible. For magnetic noise a reduction of at least a factor 2 can be obtained by replacing the BS mirror magnets and a reduction of noise coupling and of noise sources is foreseen possible (Chapter 7: new dielectric RM, identified sources). For reducing beam jitter noise a seismic isolation of EIB is necessary and a possible commercial solutions are being evaluated (Chapter 8).

The noise due to Eddy currents in the RM which was a relevant contribution to the Virgo+ budget (Figure 1.1) is now expected to be negligible, as described in [3]. This term is now included in the thermal model and it is accounted for in the Virgo+MS design curve.

Other noises which are known to give a not negligible contribution to present Virgo+ and have been not included in this noise projection are: diffused light from cryo-trap, detection tower and the Suspended Detection Bench (Section 5.5). These noises are expected to be cured with the replacement of detection output window, and reducing the light back-scattered from SDB optics (Section 5.5).

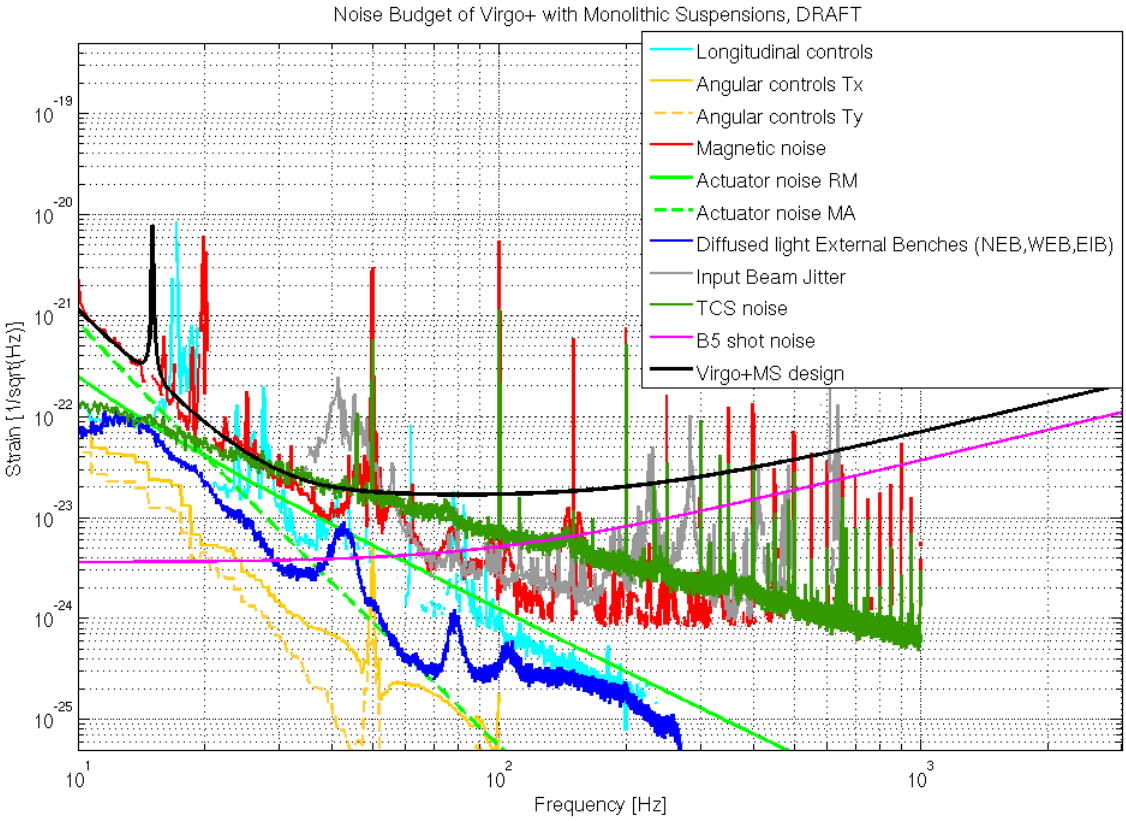

Figure 11.1. Superposition of expected noise contributions to Virgo+MS described in previous chapters.

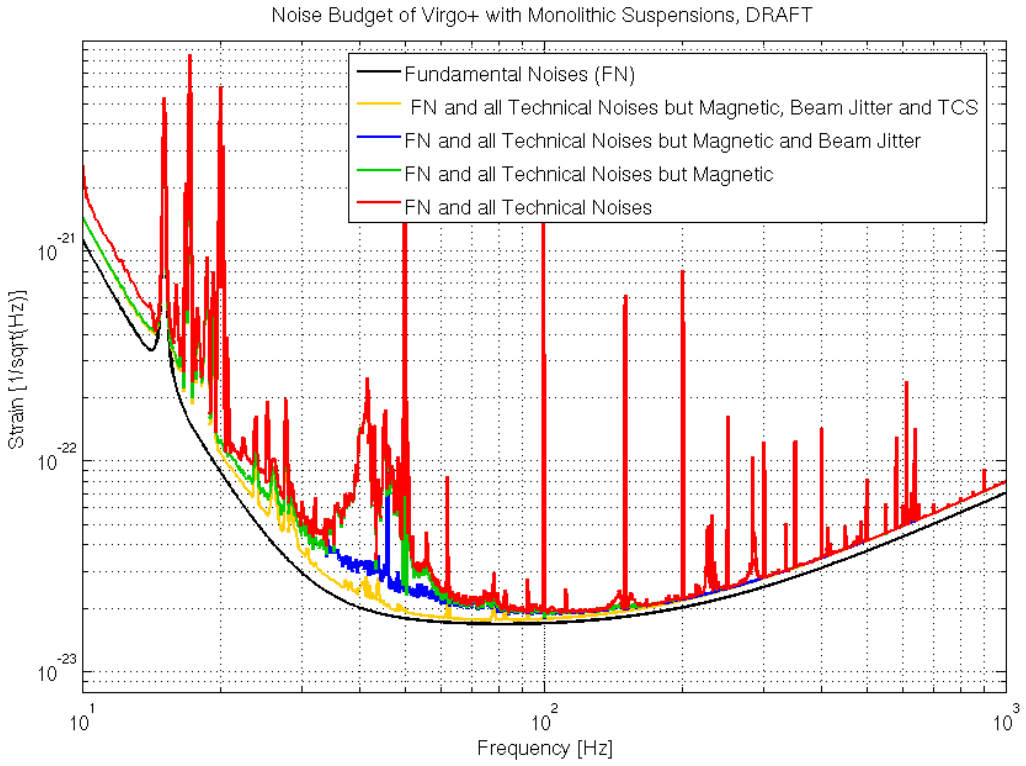

Figure 11.2. Incoherent sum of all projected noises reported in Figure 11.1 (red), compared to the design curve (black). Also shown is contribution to the total sensitivity by the TCS, magnetic and beam jitter noise.

References

[1] The Virgo Collaboration, *Commissioning report for the STAC,* VIR-0646B-09, 5 Nov. 2009.

[2] P. Puppo, *Virgo+ and Virgo+MS reference curves*, VIR-0685C-09.

[3] P. Puppo, *Virgo+MS sensitivity curve*, VIR-0639B-09.

[4] G. Vajente, *Locking and ITF performances*, VIR-0370A-09.

[5] G. Vajente, Logbook entries 24659 and 24760.

[6] V. Fafone and A. Rocchi, *TCS noise: general concepts and application to the Virgo/Virgo+ case*, VIR-0615A-09 (2009).

[7] L. Pinard, VIR-SPE-LYO-4340-0016 (2002).

[8] L. Pinard, VIR-SPE-LYO-4340-0017 (2002).

[9] L. Pinard, VIR-SPE-LYO-4340-0010 (2002).

[10] L. Pinard, VIR-SPE-LYO-4340-0011 (2002).

[11] R. Flaminio et al, *Measurement of coating absorption*, VIR-0734A-08 (2008).

[12] J.-Y. Vinet, *Thermal issues in mirrors*, TCS Workshop (Jan 2008).

[13] M. Di Paolo Emilio, V. Fafone, A. Rocchi, *TCS power stabilization status*, VIR-0368B-09 (2009).

[14] E. Tournefier, *Back-scattering by the optical benches: results from Virgo and constraints for AdV*. VIR-NOT-070A-08 (2008).

[15] B.Canuel, J.Marque, I. Fiori, E. Tournefier, *Diffused light mitigation in Virgo and constraints for Virgo+ and AdV,* VIR-0792A-09.

[16] I. Fiori, *Detection tower noise*, eLog 24130.

[17] F. Paoletti, *Case studies of environmental noise hunting and mitigation*,VIR-0509A-09.

[18] D. Huet, *Output Bench Noise*, VIR-0334A-09.

[19] B. Swinkels, *Cryo-trap bubbles noise,* eLogs 23722, 23794.

[20] A. Pasqualetti, *Bubble suppression tests*, eLogs 24571, 24642.

[21] E. Tournefier, *Baffles noise*, VIR-0350A-09.

[22] J. Marque, *Detection tower intervention*, VIR-0316A-09.

[23] A.Gennai, Actuators Noise in Virgo+ and Advanced Virgo, VIR-0146A-10, 2010.

[24] M.Bitossi, A.Gennai, D. Passuello, Low Noise DAC Selection for Advanced Virgo, VIR-0078A-10, January 20th, 2010.

[25] A. Gennai, DAC Noise Effect on Virgo Sensitivity, VIR-0006B-09, October 2nd, 2009.

[26] A. Gennai, DAC Noise Contribution to Virgo Sensitivity, VIR-0072A-08, June 6th, 2008

[27] A. Gennai, New Coil Driver Measurements, VIR-0010C-08, March 23rd, 2008.

[28] A. Gennai, Coil Driver Final Design Document, VIR-SPE-PIS-4900-121, September 30th, 2004.

[29] A.Gennai, VIR-0043A-10 New Coil Drivers (Virgo CRQ 005/2006).

[30] B. Swinkels, *Magnetic injections from the near-field*, eLog 20563.

[31] B. Swinkels, Fiori, Braccini, Paoletti, *Distortion of magnetic fields by eddy-currents in RM*, eLog 19988.

[32] Adhikari, Huet, Barsotti, Evans, *100 Hz ex-bump*, eLog 15545.

[33] B. Swinkels and I. Fiori, *50 Hz sidebands caused by MC heating*, eLog 20707.

[34] B. Swinkels and P. Popolizio, *Real culprit of magnet glitches: MC chiller*, eLog 25395.

[35] F. Paoletti, M. D'Andrea and I. Fiori, *Investigated noise of UPS CB machines*, elog 25397.

[36] E. Genin and G. Vajente, *Measurement of input jitter TF and projection*, eLog 24926.

[37] I. Fiori, *Study of EIB modes*, VIR-0322A-09.

[38] I. Fiori, *Coherence Projection EIB and LB*, eLog 25322.

[39] I. Fiori, EIB *seismic attenuation requirements for V+*, VIR-0601B-09.

[40] F.Frasconi and P.Ruggi, *Resonance damper*, eLog 22923, eLog 20540.

[41] P. Ruggi and E. Genin, *Stiffening attempts EIB*, eLog 20841.

[42] B. Canuel, R. Day, I. Fiori, E. Genin, *Stiffening and softening tests*, VIR-0411B-09.

[43] T. Bauer, F. Mul and T. Bauer, *Seismic isolation of EIB*, VIR-0602A-09.

[44] F. Mul, J. Rosier and T. Bauer, *Installation of EIB*, VIR-603A-09.

[45] E. Tournefier, *Technical noises for Virgo+: DC and AC readout*, VIR-NOT-LAP-1390-338.

[46] F. Bondu, Virgo logbook entry 14434.